

1  
2  
3 Numerical Case Study of the Aerosol-Cloud-Interactions in Warm  
4 Boundary Layer Clouds over the Eastern North Atlantic with an  
5 Interactive Chemistry Module  
6  
7  
8  
9

10 Hsiang-He Lee<sup>1</sup>, Xue Zheng<sup>1</sup>, Shaoyue Qiu<sup>1</sup>, and Yuan Wang<sup>2</sup>  
11

12  
13 <sup>1</sup>Atmospheric, Earth, and Energy Division, Lawrence Livermore National Laboratory,  
14 Livermore, CA, U.S.A.

15 <sup>2</sup>Department of Earth System Science, Stanford University, Stanford, CA, U.S.A.  
16  
17  
18  
19  
20  
21  
22  
23  
24  
25  
26  
27  
28  
29  
30  
31

32  
33 Submitted to  
34 Atmospheric Chemistry and Physics  
35

36 October 2024  
37

38 \*Corresponding author address: Dr. Hsiang-He Lee, 7000 East Avenue, Livermore, CA, 94550,  
39 U.S.A.

40 E-mail: lee1061@llnl.gov  
41  
42  
43

## Abstract

The presence of warm boundary layer stratiform clouds over the Eastern North Atlantic (ENA) region is commonly influenced by the Azores High, especially during the summer season. To investigate comprehensive aerosol-cloud interactions, this study employs the Weather Research and Forecast model coupled with a chemistry component (WRF-Chem), incorporating aerosol chemical components that are relevant with formation of cloud condensation nuclei (CCN) and accounting for aerosol spatiotemporal variation. This study focuses on aerosol indirect effects, particularly long-range transport aerosols, in the ENA region under three different weather regimes: ridge with surface high-pressure system, post-trough with surface high-pressure system, and weak trough. The WRF-Chem simulations conducted at a near **large-eddy** scale offer valuable insights into the model's performance, especially regarding its high spatial resolution in **capturing** the **mesoscale** cloud **features** across various weather regimes. Our result shows that introducing five times more aerosols to either non-precipitating or precipitating clouds significantly increases ambient CCN numbers, resulting in varying degrees of higher LWP. The substantial aerosol-cloud interaction especially occurs in the precipitating clouds and demonstrates the LWP susceptibility to changes in CCN under different regimes. Conversely, **thin**, non-rain clouds at the edges of a cloud system are prone to evaporation, exhibiting an aerosol drying effect. The aerosols released during this process transition back to the accumulation mode, facilitating future activation. This dynamic behavior is not adequately represented in prescribed-aerosol simulations.

Deleted: the Large-Eddy Simulation

Deleted: accurately

Deleted: liquid water path (LWP) and

Deleted: fraction

Deleted: ¶

## 68 1 Introduction

69 Low-level stratiform clouds are predominantly generated over oceanic regions and are  
70 categorized into three main types: warm boundary layer stratiform clouds located on the eastern  
71 side of oceanic subtropical highs, stratocumulus clouds that develop over warm western boundary  
72 currents during winter cold outbreaks, and Arctic stratus (Klein and Hartmann, 1993). Warm  
73 boundary layer stratocumulus clouds, on average, blanket around 20% of the Earth's surface  
74 annually (Wood, 2012; Warren et al., 1988). Their influence on the Earth's energy balance is  
75 substantial, primarily through their ability to reflect incoming solar radiation, resulting in  
76 significant shortwave cloud radiative effects leading to a pronounced negative net radiative effect  
77 (Chen et al., 2000; Stephens and Greenwald, 1991; Hartmann et al., 1992).

78 Research on aerosol-cloud interactions in warm boundary layer clouds has been ongoing  
79 since the 1970s. Twomey (1974) proposed that aerosols play an important role in influencing the  
80 Earth's energy budget by serving as cloud condensation nuclei (CCN). These CCN are crucial for  
81 cloud formation. A higher concentration of CCN results in the formation of clouds with a greater  
82 number of smaller-sized cloud droplets (Twomey, 1991). These smaller droplets enhance cloud  
83 albedo, known as the first indirect effect, and inhibit precipitation formation while prolonging  
84 cloud lifetime, known as the second indirect effect (Albrecht, 1989). In addition to these indirect  
85 effects, aerosol particles have direct, semi-direct, and indirect impacts on the atmosphere's energy  
86 budgets and surface, leading to changes in atmospheric stability (Lee et al., 2008). Until now, our  
87 understanding of aerosol-cloud interactions remains incomplete. In a recent review paper,  
88 Feingold et al. (2024) highlighted that the response of cloud amount (including liquid water  
89 content, spatial coverage, and cloud persistence) to aerosol perturbations is still unclear. Both  
90 positive and negative adjustments in liquid water path (LWP) and cloud fraction (CF) have been

91 observed. Increases in cloud amount (positive adjustments) are linked to rain suppression, whereas  
92 enhanced evaporation of smaller droplets and entrainment feedback tend to decrease cloud amount  
93 (negative adjustments).

94 This study focuses on warm boundary layer stratiform clouds located on the eastern side  
95 of oceanic subtropical highs, specifically targeting the area over the Eastern North Atlantic (ENA)  
96 region, where the U.S. Department of Energy (DOE) Atmospheric Radiation Measurement (ARM)  
97 program developed a ground-based user facility in the Azores archipelago (Mather and Voyles,  
98 2013). Long-term ground-based observations at the ARM ENA site, aircraft field campaigns near  
99 the Azores islands, and satellite retrievals over the ENA region provide comprehensive datasets  
100 for observational studies on aerosol-cloud interactions (Zheng et al., 2022; Zheng et al., 2023;  
101 Ghate et al., 2023; Qiu et al., 2024).

102 The presence of stratocumulus clouds over the ENA region is commonly influenced by the  
103 Azores High, also known as the Bermuda-Azores High (Rémillard and Tselioudis, 2015). This  
104 semi-permanent high-pressure system typically develops over the subtropical North Atlantic  
105 Ocean. The Azores High often brings stable and relatively dry conditions to the region, which can  
106 contribute to the formation and maintenance of stratocumulus clouds. During the summer season,  
107 the Azores High tends to strengthen and expand, leading to more persistent high-pressure  
108 conditions and often warmer, drier weather in its vicinity. Although synoptic intrusions from high  
109 latitudes are less frequent in the summer compared to the winter season (Wood et al., 2015), the  
110 ENA region still experiences synoptic variability from weak troughs during the summer months  
111 (Mechem et al., 2018; Zheng et al., 2024).

Deleted: Bermuda-



113        Leveraging the marine boundary layer cloud observations from the ARM ENA  
114        observatory, this study aims to study aerosol indirect effects (AIE), especially long-range transport  
115        aerosols, in the warm boundary layer clouds over the ENA region under three different synoptic  
116        regimes: ridge with surface high-pressure system, post-trough with surface high-pressure system,  
117        and weak trough (Mechem et al., 2018; Zheng et al., 2024). These regimes are chosen because the  
118        ARM site experiences northerly wind conditions, during the passage of troughs. This minimizes  
119        the influence of the island effect on the observations (Ghate and Cadetdu, 2019; Zheng and Miller,  
120        2022).

Deleted: , during them,

Deleted: , minimizing

121        Only a few numerical studies examined aerosol-cloud interactions in marine boundary  
122        layer clouds over this region (Zhang et al., 2021; Wang et al., 2020; Kazemirad and Miller, 2020;  
123        Christensen et al., 2024). Wang et al. (2020), for example, used the Weather Research and Forecast  
124        (WRF) model with prescribed CCN profiles to simulate perturbed long-range transport aerosol  
125        concentration for two different cases of marine boundary layer (MBL) clouds. They concluded  
126        that when long-range transport aerosol plumes penetrate down into the drizzling cloud deck, the  
127        simulations show an increase in marine cloud fractions with larger water content, supporting a  
128        positive cloud amount adjustment to CCN perturbations. Christensen et al. (2024) utilized an  
129        advanced WRF configuration integrated with a Lagrangian framework to assess the effects of  
130        aerosols on developing cloud fields across 10 case study days during the ENA field campaign and  
131        got the same conclusion. However, a limitation of these studies is that they do not account for  
132        aerosol composition acting as CCN or the changes in aerosol populations following the cloud  
133        evaporation process, even though aerosol wet removal is included in their simulations.

134        To further investigate the impacts of realistic aerosol chemical components and aerosol  
135        spatiotemporal variation on the AIE, this study adopts the WRF model coupled with a chemistry

138 component (WRF-Chem) to examine the AIE in the ENA region across different synoptic regimes.  
139 A brief description of observational data and the WRF-Chem model, as well as the configuration  
140 and numerical experiments, are given in Section 2. Simulated results are discussed in Section 3,  
141 including model evaluation, model sensitivity tests, and cloud susceptibilities. The discussion and  
142 summary are provided in Section 4.

## 143 2 Methodology

### 144 2.1 Observational data

#### 145 2.1.1 MERRA-2

146 The Modern-Era Retrospective analysis for Research and Applications, Version 2  
147 (MERRA-2), represents the latest advancement in global atmospheric reanalysis during the  
148 satellite era. Produced by NASA's Global Modeling and Assimilation Office (GMAO), it utilizes  
149 the Goddard Earth Observing System Model (GEOS) version 5.12.4 (Molod et al., 2015). The  
150 aerosol species are from the dataset, inst3\_3d\_aer\_Nv, which is an instantaneous 3-dimensional 3-  
151 hourly data collection in MERRA-2 (Modeling and Office, 2015). The dataset comprises  
152 assimilations of aerosol mixing ratio parameters at a native resolution of  $0.5^\circ$  latitude x  $0.625^\circ$   
153 longitude across 72 model layers, encompassing dust, sea salt, sulfur dioxide ( $\text{SO}_2$ ), sulfate ( $\text{SO}_4$ ),  
154 black carbon (BC), and organic carbon (OC). The data is provided every three hours, beginning  
155 at 00:00 UTC. Based on Wang et al. (2020), we also adopt MERRA-2 to drive the WRF-Chem  
156 initial and boundary conditions for this study (see [Section 2.2.2](#) for details).

Deleted: Sect.

#### 157 2.1.2 Geostationary satellite retrievals (Meteosat)

158 Cloud properties are derived from the Spinning Enhanced Visible and Infrared Imager  
159 (SEVIRI) on Meteosat-10 and Meteosat-11, which offer a spatial resolution of 3 km at nadir and

161 a half-hourly temporal resolution over the ENA region. These SEVIRI cloud products are  
162 generated using the Satellite CLOud and Radiation Property retrieval System (SatCORPS)  
163 algorithms (Painemal et al., 2021). These methods, developed by the Clouds and Earth's Radiant  
164 Energy System (CERES) project, are specifically tailored to support ARM ground-based  
165 observation sites (Minnis et al., 2011; Minnis et al., 2021). Specifically, this study adopts cloud  
166 fraction for all clouds as the observational reference over the ENA region. The adopted data have  
167 been specifically processed (e.g., solar zenith angle, cloud optical thickness, and cloud labels) and  
168 averaged to  $25 \text{ km} \times 25 \text{ km}$  (Qiu et al., 2024).

Deleted: the ARM program at

### 169 2.1.3 Aircraft observation

170 The U.S. DOE ARM Aerosol and Cloud Experiments in the Eastern North Atlantic (ACE-  
171 ENA) aircraft field campaign near the Azores islands provided extensive observations of the  
172 vertical distributions of aerosol and cloud properties (Wang et al., 2022). Intensive operational  
173 periods (IOPs) of the ACE-ENA took place in late June and July 2017, as well as January to  
174 February 2018. During the 2017 summer IOP, the ARM Aerial Facility's (AAF) Gulfstream-159  
175 (G-1) aircraft delivered precise measurements of aerosol size distribution, total aerosol number  
176 concentration, and chemical constituents both below and above cloud layers.  $\text{SO}_4$  and OC mass  
177 concentrations were measured using the Aerodyne High-Resolution Time-of-Flight Aerosol Mass  
178 Spectrometer (HR-ToF-AMS), while refractory BC was measured by the Single Particle Soot  
179 Photometer (SP2). Detailed information about each instrument is available on the ARM website  
180 (<https://www.arm.gov/research/campaigns/aaf2017ace-ena>). In this study, aircraft measurements  
181 of  $\text{SO}_4$ , OC, and BC from 19 July 2017, are utilized to assess the simulated aerosol vertical profile.  
182 However, uncertainties arising from the measurements and spatiotemporal sampling strategies  
183 may hinder direct comparisons of absolute values between the observations and modeled results.

#### 185 2.1.4 ARM ground-based observations

186 The DOE ARM ground-based instruments deployed on Graciosa Island in the Azores  
187 archipelago provide comprehensive measurement of aerosols, clouds, radiation, atmospheric  
188 boundary layer, and other atmospheric properties. In this study, LWP is retrieved from the  
189 brightness temperature measured by the microwave radiometer (MWR) at 23.8 and 31.4 GHz  
190 (Liljegren et al., 2001) and used for model evaluation. The temperature and moisture profiles are  
191 from the interpolated sonde data, derived from the radiosonde measurement.

### 192 2.2 The model

#### 193 2.2.1 WRF-Chem

194 The Weather Research and Forecasting (WRF) model version 4.4.2 (Skamarock et al.,  
195 2021) coupled with a chemistry component (WRF-Chem) (Grell et al., 2005) is used in this study.  
196 The standard WRF-Chem permits the simulation of the combined direct, indirect, and semi-direct  
197 effects of aerosols (Grell et al., 2005; Fast et al., 2006; Chapman et al., 2009). WRF-Chem version  
198 4.4.2 has sophisticated packages to represent chemistry processes (i.e., gas-phase reaction, gas-to-  
199 particle conversion, coagulation, etc.) and aerosol size and composition (Binkowski and Shankar,  
200 1995). In this study, the Regional Acid Deposition Model version 2 (RADM2) photochemical  
201 mechanism (Stockwell et al., 1997) is integrated alongside the Modal Aerosol Dynamics Model  
202 for Europe (MADE) and the Secondary Organic Aerosol Model (SORGAM) (Ackermann et al.,  
203 1998; Schell et al., 2001) to simulate atmospheric chemistry and the evolution of anthropogenic  
204 aerosols. MADE/SORGAM adopts a modal approach to represent the aerosol size distribution,  
205 predicting mass and number concentrations across three aerosol modes (Aiken, accumulation, and  
206 coarse). MADE/SORGAM has inorganic, organic, and secondary organic aerosols and contain  
207 aerosol formation processes including nucleation, condensation, and coagulation. WRF-Chem

Deleted: liquid water path (

Deleted: )

210 tracks the number of particles and the mass of chemical compounds (e.g.,  $\text{SO}_4^{2-}$ ,  $\text{NH}_4^+$ ,  $\text{NO}_3^-$ ,  $\text{Na}^+$ ,  
211  $\text{Cl}^-$  etc.) in each aerosol mode, including both interstitial aerosols and aerosols present in liquid  
212 water (the sum of cloud and rain), as prognostic variables.

213 The size, composition, and mixing state of aerosols significantly influence their capability  
214 to activate as CCN (Zaveri et al., 2010). A physically based aerosol activation parameterization  
215 scheme has been developed for climate models to simulate CCN concentration accurately and  
216 efficiently (Abdul-Razzak and Ghan, 2000). This aerosol activation parameterization was initially  
217 designed for a single aerosol type with a lognormal size distribution. Then, they expanded this  
218 parameterization to accommodate multiple externally mixed lognormal modes, with each mode  
219 consisting of both soluble and insoluble materials internally mixed. However, WRF-Chem  
220 (MADE/SORGAM) chemistry package adopts this global internal mixing assumption, where all  
221 particles within a log-normal mode within the same grid cell are instantly combined, resulting in  
222 the same chemical composition. This instantaneous internal mixing assumption modifies the  
223 optical and chemical characteristics of particles in WRF-Chem simulations, potentially impacting  
224 aerosol-cloud interactions, such as aerosol activation as CCN (Zhang et al., 2014).

### 225 2.2.2 The configuration

226 Our focus in this study is to examine aerosol-cloud interactions close to the scale of large-  
227 eddy simulation (LES) over the ARM ENA site. We use WRF-Chem with a full chemistry  
228 package involving sophisticated gaseous and aqueous chemical processing calculations and dry  
229 and wet depositions. The numerical simulations are employed with 4 domains ~~consisting of 4~~  
230 horizontal resolutions of 5 km, 1.67 km, 0.56 km, and 0.19 km, respectively (Fig. 1), with one-  
231 way nesting. ~~There are  $550 \times 530$  grids for D1,  $451 \times 430$  grids for D2,  $553 \times 532$  grids for D3,~~  
232 ~~and  $553 \times 532$  grids for D4. The domain size of domain 4 is about 1 degree which is similar to~~

Deleted: with

the spacing resolution of global climate models. Seventy-five vertically staggered layers are stretched to have a higher resolution near the surface based on a terrain-following pressure coordinate system. With this setup, the model has roughly 24 model layers in the boundary layer (~2000 m). The time step is 30 and 10 seconds for advection and physics calculation for domains 1 and 2, respectively. The nesting inner domains 3 and 4 have the time step of 3 seconds and 1 second, respectively. The physics schemes adopted in the simulations are listed in Table 1. The initial and boundary meteorological conditions are taken from ERA5, developed by the Copernicus Climate Change Service (C3S) at ECMWF (European Centre for Medium-Range Weather), stands as the fifth generation of ECMWF atmospheric reanalysis, spanning from January 1940 to the present day (Hersbach et al., 2023). This comprehensive dataset offers hourly estimates of numerous atmospheric, land, and oceanic climate variables, covering the entirety of Earth on a 31 km grid. The atmospheric component is resolved using 137 levels, spanning from the surface up to 80 km in height.

Deleted: the

Deleted: 31km

The computational expense of conducting a 4-domain WRF-Chem simulation, particularly with LES resolution, is exceedingly high. To mitigate this, we execute WRF solely for the two outer domains (d01 and d02), leveraging the WRF downscaling module (ndown) (Skamarock et al., 2008) to generate meteorological initial and boundary conditions for domain 3. As a result, we only need to perform WRF-Chem simulations for the two inner domains (d03 and d04), leading to an almost 50% reduction in total computational costs (compared to the original 4-domain run, which had a throughput of 4 hours per day using 1080 cores). It is important to note that a high temporal frequency for domain 3 boundary conditions is essential due to its fine horizontal resolution (0.56 km). In this context, we update the boundary condition every 5 minutes for domain 3.

259 To enhance the realism of aerosol mass simulation in remote marine regions, such as the  
260 ENA site, we account for major aerosol species (BC, OC, and SO<sub>4</sub>), as well as SO<sub>2</sub>, from MERRA-  
261 2 into the boundary conditions of domain 3. Aerosols in the initial condition are introduced into  
262 the restart file (wrfirst) following a one-hour initial run, rather than in the initial condition file  
263 (wrfinput), to address certain numerical challenges. According to the emission setup for  
264 MADE/SORGAM, we assume that the Aiken mode and the accumulation mode account for 20%  
265 and 80% of the aerosol mass (BC and OC), respectively (Tuccella et al., 2012). Conversely, for  
266 SO<sub>4</sub>, 80% is allocated to the Aiken mode and 20% to the accumulation mode, reflecting the faster  
267 growth rate of SO<sub>4</sub> and a longer duration of growth from the domain 3 boundary. Because  
268 MERRA-2 only provides aerosol mass, the aerosol number concentrations for different aerosol  
269 species are estimated with the density assumption of BC (1.7 g cm<sup>-3</sup>), OC (1.0 g cm<sup>-3</sup>) and SO<sub>4</sub>  
270 (1.77 g cm<sup>-3</sup>) based on Liu et al. (2012). Aerosol optical depth retrieved from satellite remote  
271 sensing can offer valuable information for comparison; however, it may be subject to high bias in  
272 our study cases due to cloud cover.

Deleted: the

273 It is common to consider that the ENA region is an unpolluted area because it is far away  
274 from the anthropogenic pollution sources. Besides long-range transport aerosols, two local aerosol  
275 sources, dimethyl sulfide (DMS) and sea salts, are also important for the aerosol budget. Kazil et  
276 al. (2011) pointed that the observed DMS flux from the ocean in the VOCALS-REx field campaign  
277 over the Southeast Pacific can support a nucleation source of aerosol. DMS oxidation by nitrate  
278 (NO<sub>3</sub>) produces SO<sub>2</sub> and then increases SO<sub>4</sub> concentration (Toon et al., 1987). Since we adapted  
279 SO<sub>2</sub> and SO<sub>4</sub> concentration from MERRA-2 in the initial and boundary conditions, we did not  
280 double count DMS emissions in our simulations. As a result, chemical species emissions, except  
281 for sea salt, are excluded from the simulations. The emission of sea salt particles is parameterized

283 using the method outlined by Clarke et al. (2006) in WRF-Chem. ~~Sea salt emissions are driven by~~  
 284 ~~surface wind speed. The simulated surface wind speed aligns closely with ERA-5 data; however,~~  
 285 ~~the sea salt concentration is only one-third of the value found in the MERRA-2 analysis. To~~  
 286 ~~improve the alignment with the sea salt aerosol concentration observed in the MERRA-2~~  
 287 ~~reanalysis, we~~ adjust the parameter factor for sea salt ~~emissions~~ to three times the original estimate  
 288 ~~(further comparison can be found in Section 3).~~

Deleted: We

Deleted: the

Deleted: emission

Deleted: higher than

Deleted: to achieve better agreement with the sea salt aerosol variation in MERRA-2 reanalysis.

## 289 2.3 Study cases and numerical experiment design

290 We select three specific study cases to assess the impact of long-range transport aerosols on  
 291 warm boundary layer clouds, with each case representing a typical meteorological regime observed  
 292 over the ENA site. The first case, dated 1 July 2016, exhibits the formation of overcast  
 293 stratocumulus clouds (Fig. 2a) within a meteorological regime characterized by a ridge system in  
 294 the free troposphere and a high-pressure system near the surface (Fig. 2d). Predominant  
 295 northwesterly and northerly winds in the area of the ARM ENA site coincide with the presence of  
 296 long-range transport aerosols, commonly found along the periphery of the high surface pressure  
 297 system (Logan et al., 2014; Gallo et al., 2023).

298 The second case on 19 July 2017 is a stratocumulus cloud case (Fig. 2b) within a post-  
 299 trough regime featuring a high surface pressure under the influence of a trough system (Fig. 2e).  
 300 Following the trough passage, robust northwesterly winds facilitated the influx of long-range  
 301 transport aerosols into the region, which then shifted to northerly winds as the trough moved away.  
 302 Because the ACE-ENA aircraft field campaign ~~intensive operations period (IOP) was during this~~  
 303 time, ~~aircraft~~ aerosol observational data can be used to evaluate the model performance for this  
 304 case.

Deleted: ran on

Deleted: more



313 Finally, the third case, dated 23 August 2019, occurred during a period of weak trough  
314 activity (Fig. 2f). Here, we noted the presence of broken, thicker stratocumulus clouds, often  
315 accompanied by deeper cloud formations (Fig. 2c). Long-range transport aerosols were again  
316 observed, primarily carried by northwesterly and northerly winds, albeit with weaker surface wind  
317 speeds compared to the preceding two cases.

318 All simulations start at 12 UTC on the preceding day of the study case, spanning a duration  
319 of 36 hours, with the initial 12 hours dedicated to spin-up. Again, aerosols in the initial condition  
320 are introduced into the restart file after one-hour initial run (i.e., 13 UTC). The three  
321 aforementioned cases, labeled as control cases (20160701\_control, 20170719\_control, and  
322 20190823\_control), are utilized to examine the behavior of warm boundary layer clouds under  
323 diverse meteorological conditions. Additionally, we formulated three perturbed cases  
324 (20160701\_perturbed, 20170719\_perturbed, and 20190823\_perturbed) by amplifying aerosol  
325 concentrations in both initial and boundary conditions, as well as sea salt emissions, by a factor of  
326 five relative to each control case. These control cases represent clean conditions, with near-surface  
327 CCN concentrations below  $100\text{ cm}^{-3}$  at the ARM ENA site. A comparison between the control  
328 and perturbed cases elucidates the sensitivity of warm boundary layer clouds to aerosol  
329 enhancements under varying meteorological conditions, thereby contributing to a deeper  
330 understanding of cloud microphysics processes under varying atmospheric dynamics.

## 311 3 Results

### 312 3.1 Model evaluation

#### 313 3.1.1 Meteorological conditions

314 Figures 2g, 2h, and 2i display the model-simulated LWP in the control runs over domain 3  
315 and 4. The modeled LWP is calculated in-cloud LWP only. The simulations with fine spatial

Deleted: liquid water path (

Deleted: )

Deleted: the

339 resolution effectively capture synoptic frontal systems and cloud features, particularly when  
340 compared to the cloud images from the Meteosat satellite (Figs. 2a, 2b, and 2c). Thin, uniform  
341 stratocumulus clouds on 1 July 2016 are simulated in 20160701\_control, while the solid  
342 stratocumulus and frontal system on 19 July 2017 are also well captured in 20170719\_control.  
343 Broken stratocumulus clouds on 23 August 2019 are reproduced in the simulation of  
344 20190823\_control. Figures 2j, 2k, and 2l display the model-simulated LWP in the perturbed runs.  
345 The overcast stratocumulus clouds are simulated better in 20160701\_perturbed (Fig. 2j), which  
346 more accurately reflects reality.

347 The control runs serve as a basis for comparing the boundary layer structure against the  
348 interpolated soundings obtained from the ARM ENA site. Figure 3 depicts the comparison,  
349 showing the simulated air temperature aligning closely with the observed values. However, on 1  
350 July 2016, the model (20160701\_control) displays a warm bias in capturing the temperature  
351 inversion (Figs. 3a and 3b), with the simulated inversion layer situated approximately 200-300 m  
352 lower than observed, during the whole study period. Potential temperature and relative humidity  
353 have consistent performance as illustrated in Figs. S1b and S2b, respectively. While the model  
354 indicates high relative humidity (> 90%) within 1000 m, observations show this extending up to  
355 ~1200 m.

356 For the 19 July 2017 case, the model (20170719\_control) successfully represents the  
357 diurnal cycle of temperature vertical gradient within 1000 m height. However, compared to  
358 observations, the model does not catch the inversion at 1500 m height near the noon time and  
359 shows a warm bias in the model's simulated temperature (Figs. 3c and 3d). The model simulation  
360 also tends to depict drier conditions in the evening compared to the observation (Figs. S3c and  
361 S3d).

Deleted: Figures

Deleted: depict

Deleted: . Relative

Deleted: has

Deleted: and shows

Deleted: S1a

Deleted: S1b

Deleted: Moving to

Deleted: S1c

Deleted: S1d

372 On 23 August 2019, characterized by a weak trough regime and higher boundary layer  
 373 height, the simulation of 20190823\_control accurately captures warm and moist air advection in  
 374 the morning but ~~has difficulty in maintaining~~ fidelity in the late afternoon. Notably, the lower  
 375 troposphere becomes excessively warm and dry after ~~17 Z local time~~ compared to observations  
 376 (Figs. 3e, 3f, ~~S2e, S2f, S3e, and S3f~~).

Deleted: struggles to maintain

Deleted: 18 UTC

Deleted: S1e

Deleted: S1f

377 In general, all simulations effectively capture large-scale conditions and cloud features  
 378 (Fig. 2) across different synoptic regimes but do not accurately represent temperature inversions  
 379 and air advection patterns. Discrepancies are noted in the simulated boundary layer height, which  
 380 is lower, and the inversion is weaker than actual observations. Furthermore, the discrepancies tend  
 381 to increase in the later stage of simulation.

### 382 3.1.2 Aerosol evolution

383 As mentioned in Section 2.2.2, we incorporate major aerosol species (BC, OC, and SO<sub>4</sub>),  
 384 from MERRA-2 into the domain 3 initial (in the restart file at 13 UTC) and boundary conditions  
 385 to enhance the realism of aerosol simulation. Figure 4 shows time-series SO<sub>4</sub> vertical profiles  
 386 from both MERRA-2 and WRF-Chem for three study cases. Here, we demonstrate the time  
 387 evolution of SO<sub>4</sub>. ~~This species~~ is the main aerosol component among the three introduced aerosol  
 388 species, about 60~80% of total aerosol mass, in the initial conditions.

Deleted: because SO<sub>4</sub>

389 Compared to the MERRA-2 data, 20160701\_control well captures the long-range transport  
 390 SO<sub>4</sub> between 1000 m and 2000 m, which is above the cloud deck, on 1 July 2016 (Figs. 4a and 4b).  
 391 The observed high BC and OC are also concentrated in this layer (Figs. ~~S4a and S5a~~), as well as  
 392 simulated ones (Figs. ~~S4b and S5b~~). ~~Figures~~ 4c and 4e show two MERRA-2 time-series vertical  
 393 distributions of SO<sub>4</sub> on 19 July 2017 and 23 August 2019, both showing low-altitude (below 1500  
 394 m) aerosol plumes. On 19 July 2017, the concentrations of BC and OC showed two peaks – one

Deleted: S2a

Deleted: S3a

Deleted: S2b

Deleted: S3b). Figure

404 near the surface and another above 1500 m in the free troposphere (Figs. [S4c](#) and [S5c](#)). This  
 405 pattern indicates the presence of a biomass-burning signature in the plume on that day (Wang et  
 406 al., 2020). While the simulation of 20170719\_control did not capture the near surface BC, OC,  
 407 and SO<sub>4</sub> concentration after [11 Z local time](#) on 19 July 2017 (Figs. [S4d](#), [S5d](#), and 4d). It is because  
 408 in the case of the post-tough regime, the wind direction changes from northwesterly to northerly  
 409 when the trough moved away, [and](#) the aerosol plume in domain 3 did not propagate into domain 4  
 410 when the wind direction [changed](#) (figure not shown). However, the simulation of  
 411 20170719\_control still captures the BC and OC plumes in the free troposphere (above 2000 m  
 412 height) (Figs. [S4d](#) and [S5d](#)).

413 Aircraft observations during [ACE-ENA](#) provide more accurate depictions of aerosol  
 414 vertical distribution and aerosol layer heights, with differentiation of aerosol type. Figure 5a shows  
 415 the vertical distribution of aerosol mass concentrations averaged over the flights on 19 July 2017.  
 416 BC, OC and SO<sub>4</sub> all increase with height above clouds (~1000 m), indicating downward  
 417 propagation of aerosol plumes and possible interaction with MBL clouds (600 – 1000 m). Here,  
 418 we also see that high SO<sub>4</sub> in the free troposphere, [similar to](#) MERRA-2, but the model  
 419 underestimates the OC concentration in the free troposphere. On the other hand, within the MBL,  
 420 there is a much higher concentration of SO<sub>4</sub> in the MBL than those of BC and OC in the  
 421 observations. This phenomenon is also captured by the WRF-Chem simulation (Fig. 5b), but the  
 422 model did not capture the magnitude of [the](#) SO<sub>4</sub> concentration.

423 Similarly, for the case of [20190823](#), within the low boundary layer, there is a much higher  
 424 concentration of SO<sub>4</sub> in the low boundary layer (Fig. 4e). After [the noon time](#) on 23 August 2019,  
 425 BC and OC show both high-altitude plumes and low-altitude plumes approaching into the domain,  
 426 which indicate potentially two different aerosol sources (Figs. [S4e](#) and [S5e](#)). Again, while the

Deleted: S2c

Deleted: S3c

Deleted: 12 UTC

Deleted: S2d, S3d

Deleted: winds

Deleted: the

Deleted: the

Deleted: change

Deleted: S2d

Deleted: S3d

Deleted: the

Deleted: same as the data in

Deleted: 23 August 2019

Deleted: 12 UTC

Deleted: S2c

Deleted: S3c

443 simulation of 20190823\_control well captures the time evolution of aerosol plume, the boundary  
 444 of high-altitude plumes and low-altitude plumes appears 300 m lower in the simulations (~600 m  
 445 in altitude; Figs. S4f and S5f) compared to the observations (~900 m in altitude).

Deleted: S2f

Deleted: S3f

446 Sea salt particles serve as an important source of CCN over the ocean, particularly in  
 447 unpolluted conditions. However, due to their larger particle size, sea salt particles tend to  
 448 accumulate near the ocean surface and are swiftly removed by dry deposition and sedimentation  
 449 processes (Chin et al., 2002). The simulation of 20160701\_control (Figs. S6a and S6b) accurately  
 450 reproduces sea salt concentrations, both in magnitude and vertical distribution, consistent with  
 451 observations, same as the case of 20170719 (Figs. S6c and S6d). Nevertheless, the model  
 452 encounters difficulties in simulating sea salt concentrations for the case of 23 August 2019 (Figs.  
 453 S5e and S5f), corresponding to a weak-trough system (Fig. 2c). Although the simulated surface  
 454 wind speed matches well with ERA-5 (Fig. S7), the underestimation of sea salt concentrations may  
 455 be attributed to limitations in the emission parameterization, which is overly reliant on surface  
 456 wind speed (Gong, 2003).

Deleted: salts

Deleted: As discussed in Section 2.2, we adjusted the parameter factor to three times its original value to better align with the MERRA-2 dataset.

Deleted: S4a

Deleted: S4b

Deleted: S4c

Deleted: S4d

Deleted: S4e

Deleted: S4f

Deleted: Sea salt emissions in WRF-Chem are driven by surface wind speed; however,

Deleted: S5). Hence, underestimated

Deleted: stem from inadequacies in

Deleted: excessively determined by the

### 457 3.1.3 Cloud properties

458 In Fig. 6, we observe a comparison between the simulated results and observations of LWP  
 459 and CF at different spatial scales (4 km- and domain-average, respectively) to leverage the  
 460 spatiotemporal advantages offered by both sets of observations. The ARM ground-based  
 461 instrument recorded an LWP of over 400 g m<sup>-2</sup> during the nighttime with drizzle droplets reaching  
 462 to the surface on 1 July 2016 (Fig. 6a). As the sunrise (around 6 Z local time), the LWP decreases  
 463 to a range of about 100 g m<sup>-2</sup>, and then increases again to 600 g m<sup>-2</sup> after 21 Z local time.

Deleted: drizzles

Deleted: UTC

Deleted: ,

Deleted: 22 UTC

485 To compare with the ARM ground-based observations, the WRF-Chem simulated result is  
 486 averaged over  $20 \times 20$  grids centered on the Azores, which corresponds to an approximate  
 487 resolution of 4 km (Fig. 6a). Overall, the control run generates a thin cloud layer with an  
 488 underestimated LWP during the nighttime, capturing only 10-20% of the observed LWP. The  
 489 simulated clouds are more consistent with the observations during the daytime, especially in the  
 490 perturbed run. However, it is important to note that the LWP retrieved by MWR experiences  
 491 significant uncertainties during drizzling or precipitating conditions. This is primarily due to the  
 492 scattering effects of large raindrops and raindrops accumulating on the instrument's radome, which  
 493 can result in an overestimation of LWP (Tian et al., 2019; Cadeddu et al., 2020).

494 Figure 6b depicts the comparison of CF between observations and WRF-Chem. The CF  
 495 values obtained from Meteosat are close to 1, indicating a solid cloud field. In contrast, the CF  
 496 simulated by 20160701\_control range between 0.5 and 0.9 on a domain-averaged scale. Similar  
 497 to the LWP results, the simulated CFs from 20160701\_control exhibit a diurnal cycle, with higher  
 498 values during the nighttime and lower values during the daytime. Due to the thinner clouds  
 499 simulated in 20160701\_control based on LWP, the modeled CF is 40-60% lower than the  
 500 observation in the afternoon, indicating that clouds dissipate more quickly in the control run.  
 501 Conversely, the 20160701\_perturbed scenario demonstrates improved performance in both LWP  
 502 and CF. This indicates that the 20160701 case is sensitive to aerosol variations, with the CCN  
 503 number being too low in the control run.

504 Compared to a ridge system like the case of 20160701, the WRF-Chem model has  
 505 difficulty in capturing the warm boundary layer clouds under a regime characterized by a post-  
 506 trough system (20170719) or a weak trough system (20190823). Compared to the observations,  
 507 the simulated LWP in 20170719\_control is about 30% of the observed value (Fig. 6c. In contrast,

Deleted: model

Deleted: .

Deleted: WRF-Chem

Deleted: WRF-Chem

Deleted: WRF-Chem

Deleted: model.

Deleted: is harder to capture

Deleted: like the case of

Deleted: like the case of

517 the simulated CF performs better, reaching about 75% of the observed value (Fig. 6d). The  
 518 discrepancy between the modeled results and observations may arise from delayed moisture  
 519 transfer from the outer domain or insufficient vertical resolution. In this instance, the cloud  
 520 systems move quickly under the post-trough weather regime. A 5-minute moisture input from the  
 521 boundary condition using WRF downscaling (ndown) may not be sufficient to transport moisture  
 522 into the inner domain, making it difficult for the model to develop thicker marine stratocumulus  
 523 clouds, especially for such high spacing resolution. On the other hand, in another ongoing project,  
 524 we increased the vertical layers to 99, which is to double vertical layers below 2km. However, the  
 525 test with 99 levels only slightly improves the cloud cover and LWP. The estimated LWP  
 526 susceptibility shows little to no change. The insignificant improvement indicates even higher  
 527 resolution is needed to fully simulate the cloud processes near the sharp boundary layer inversion  
 528 for these solid stratocumulus cloud layer. Another possible reason is that the 6th Order Horizontal  
 529 Diffusion used in the study (diff\_6th\_opt = 2) rapidly dissipates marine stratiform clouds,  
 530 especially in the high spacing resolution (Knievel et al., 2007). It is worth noting that Christensen  
 531 et al. (2024) conducted sensitivity tests using various shallow cumulus and microphysics schemes,  
 532 and the different combinations of these schemes had a substantial impact on the simulated cloud  
 533 amount as well.

534 Moving to the case of 20190823, overall, compared to the observations, the control run  
 535 captures LWP and CF slightly better, especially in the domain-averaged scale (Figs. 6e and 6f).  
 536 Based on the LWP observed from ARM, there are two systems passing in the area, one between 5  
 537 Z to 13 Z local time and the other between 17 Z to 22 Z local time on 23 August 2019, (high ARM  
 538 LWP in Fig. 6e). The simulation of 20190823\_control captures the first system, but slightly  
 539 underestimates LWP; however, the model misses the second system. The model simulated CFs

Deleted: have observed that increasing

Deleted: significantly enhances the simulated

Deleted: amount (figure not shown).

Deleted: is easy to break down the

Deleted: to mention

Deleted: model

Deleted: 7 UTC

Deleted: 14 UTC

Deleted: 18 UTC

Deleted: 24 UTC

Deleted: .

Deleted: a little bit

552 also match well with Meteosat (Fig. 6f). Only after 17 Z, the model misses catching the second  
553 system. The CFs drops 50 – 70 % compared to the observations.

Deleted: 18 UTC

554 The underestimation of LWP and CF in model simulations leads to insufficient longwave  
555 cooling at the cloud top. This reduced cooling weakens cloud-top entrainment, resulting in a less  
556 pronounced boundary layer inversion and a shallower boundary layer height identified in Section  
557 3.1.1. This creates a negative feedback loop, where the initial inaccuracies in cloud properties  
558 affect boundary layer dynamics (Zheng et al., 2021). On the other hand, in the perturbed runs, the  
559 results show an adjustment in the amounts of LWP and CF, aligning more closely with the  
560 observations. This suggests that the CCN number is underestimated in the control runs (more  
561 discussion in Section 3.3). The model's response to aerosol changes highlights its capability for  
562 studying aerosol-cloud interactions.

Deleted: the cloud layer from the

Deleted: results in

Deleted: , which may contribute to

Deleted: weaker

Deleted: depth

Deleted: the previous section (

Deleted: )

## 563 3.2 Aerosol composition and activation

564 The advantage of utilizing WRF-Chem to investigate aerosol-cloud interactions stems from  
565 its capability to simulate the spatiotemporal distribution of CCN. This modeling is based on  
566 various aerosol components and their sizes, as well as their dynamic responses to wet removal  
567 processes associated with clouds and precipitation. In traditional simulations that rely on fixed or  
568 prescribed aerosol distributions, accurately representing these factors can be particularly  
569 challenging. WRF-Chem, however, allows for a more nuanced understanding by dynamically  
570 modeling how aerosol populations evolve over time, especially after cloud evaporation processes.  
571 During the evaporation process, the reduction in cloud water can lead to a re-entrainment of  
572 aerosols back into the atmosphere, altering their concentration and properties. This change can  
573 affect subsequent cloud formation and precipitation patterns, highlighting the importance of  
574 capturing these interactions for reliable predictions.



583 In this section, we concentrate on aerosol activation, considering its size and chemical  
584 composition across three different cases. The following section will discuss the aerosol indirect  
585 effect and how changes in cloud properties feedback into the aerosol population and its activation  
586 capability.

587 In Fig. 7a, the blue solid line and blue dashed line represent the vertical profiles of total  
588 aerosol number concentration (including Aiken mode and accumulation mode) and aerosol number  
589 concentration of the Aiken mode, respectively. These profiles are averaged over domain 4 on 1  
590 July 2016. The environment shown in the figure is characterized by its cleanliness, with a total  
591 aerosol number concentration below the cloud top (approximately 1000 m in height) measuring  
592 less than  $300 \text{ cm}^{-3}$ . In the 20160701\_control simulation, the total aerosol number is low, and  
593 approximately 70% of the total aerosol numbers belong to the Aiken mode. According to the study  
594 conducted by McCoy et al. (2024), which utilized aerosol number concentration measurements  
595 from ARM airborne observations on 15 July 2017, it was found that the ratio of the Aiken mode  
596 to the total aerosol number was approximately 50-60% within an altitude of 1000 m. Compared  
597 to this observational analysis, our simulations generate an overabundance of small-sized aerosols,  
598 which result in a low concentration of CCN. This discrepancy arises from the assumptions made  
599 when constructing the aerosol initial and boundary conditions (80% for Aiken mode and 20% for  
600 accumulation mode  $\text{SO}_4$ ).

601 The CCN calculation presented in Fig. 7a is based on the Köhler theory, which considers  
602 both the aerosol size (curvature effect) and the chemical composition (solution effect) to estimate  
603 the theoretical CCN number concentration at different supersaturations. Below 1.0%  
604 supersaturation, the CCN number concentration is found to be 42% of the total number of aerosol  
605 number (could be estimated from 100% of accumulation mode and 16% of Aiken mode) (Fig.

Deleted: the

Deleted: , which is the assumptions regarding the aerosol mode ratio of  $\text{SO}_4$

Deleted: Under

610 ~~S8a~~). In the simulation of 20160701\_control, the CCN number concentration ~~below~~ 0.2% (0.5%)  
 611 supersaturation is only 11% (25%) of the total aerosol number, which is lower than the  
 612 observations reported in Wang et al. (2020), where the observed CCN number concentration under  
 613 0.35% supersaturation was approximately 25% of the total aerosol number. Even though SO<sub>4</sub> is  
 614 the dominant chemical component, accounting for nearly 50% (as shown in Figs. ~~8b~~ and ~~8c~~), the  
 615 presence of an excessive number of Aiken mode aerosols may be the primary reason for the low  
 616 activation rate. The curvature effect caused by these Aiken mode aerosols hinders their ability to  
 617 act as CCN effectively.

Deleted: S6a

Deleted: under

Deleted: 7b

Deleted: 7c

618 In the simulation of 20170719\_control, the most aerosols ~~are~~ within a height of 1000 m,  
 619 which is also the cloud layer (Fig. 7d). The average aerosol number concentration across the entire  
 620 domain is measured to be 1286 cm<sup>-3</sup> within a height of 2000 m and the Aiken mode is 80% of the  
 621 total aerosol number in this case. The chemical composition of aerosols in the 20170719\_control  
 622 mainly is SO<sub>4</sub> ~~with the other species exhibiting lower concentrations (Figs. 7e and 7f)~~. This  
 623 variation in vertical distribution leads to more aerosols being activated under the cloud top at a  
 624 height of 1500 m. This is attributed to the presence of a peak value of accumulation mode aerosols  
 625 and SO<sub>4</sub> at this height.

Deleted: , and "others" (like sea salts) is second (Figs.

626 Because of ~~the high number concentration of simulated~~ Aiken mode aerosols, overall, the  
 627 activation rate is low. ~~Below~~ 1.0% supersaturation, the CCN number concentration is estimated  
 628 to be 25% of the total aerosol number. This could be a result of 100% of the accumulation mode  
 629 aerosols and 7% of the Aiken mode aerosols contributing to the CCN population (Fig. ~~S8c~~). The  
 630 CCN number concentration ~~below~~ 0.2% (0.5%) supersaturation is only 4% (12%) of the total  
 631 aerosol number.

Deleted: in this simulation

Deleted: Under

Deleted: S6c

Deleted: under

641 Among the three cases studied, the case of 20190823 stands out as the most polluted case,  
 642 but the aerosol component and vertical distribution are close to the case of 20170719 (Figs. 7c and  
 643 7i). The average aerosol number concentration across the entire domain is measured to be 1850  
 644  $\text{cm}^{-3}$  within a height of 2000 m. The Aiken mode aerosols are also high and contribute to more  
 645 than 75% of the total aerosol number in this case (Figs. 7g and S8e). The large  $\text{SO}_4$  species  
 646 concentration also leads to more aerosols being activated under the cloud top at a height of 2000  
 647 m. The CCN number concentration below 0.2% (0.5%) supersaturation is only 6% (17%) of the  
 648 total aerosol number, slightly better than the case of 20170719.

Deleted: S6e). High  $\text{SO}_4$  component

Deleted: under

649 The cloud droplet numbers observed in the three cases fall within the range of CCN  
 650 numbers below 0.1% and 0.2% supersaturation. Therefore, in the subsequent sections, we utilize  
 651 the CCN number concentration below 0.2% supersaturation as a representative of the CCN  
 652 activation rate.

Deleted: under

Deleted: under

### 653 3.3 Cloud responses to aerosol perturbations

654 Figure 8 illustrates the comparison of time series profiles of cloud water content (CWC)  
 655 and CCN number concentration below 0.2% supersaturation between the control runs and  
 656 perturbed runs. This figure also demonstrates the CCN spatiotemporal variation in our  
 657 simulations. Specifically, for the case of 20160701, it is evident that the CWC in  
 658 20160701\_perturbed exhibits a positive response to increased CCN compared to the CWC in  
 659 20160701\_control. This result aligns with most WRF studies that use fixed or prescribed CCN  
 660 numbers to investigate aerosol-cloud interactions (Wang et al., 2020; Christensen et al., 2024).

Deleted: under

Deleted: the

Deleted: of

Deleted:

661 Echoing the insufficient longwave cooling at the cloud top due to the underestimation of  
 662 LWP and CF in model simulations discussed in Section 3.1.3, Terai et al. (2014) also observed

671 weak cloud-top entrainment in their study of five pockets of open cells, using aircraft data from  
 672 the VOCALS Regional Experiment (VOCALS-REx). Their research indicated that clouds tend to  
 673 break up easily in the absence of aerosols, characteristic of a pristine environment. Consistent  
 674 with their findings, our study demonstrates that in-cloud collision-coalescence processes  
 675 effectively remove aerosols, particularly because of the wider range of cloud droplet sizes present  
 676 in a clean environment (i.e., the control runs) (Table 2). Even in the control run for 20160701, our  
 677 results indicate that broken open cell clouds in a pristine environment struggle to develop into  
 678 closed clouds.

679 Figure 9a depicts the time series of domain-averaged LWP, encompassing both cloud and  
 680 rain, and CCN number concentration below 0.2% supersaturation for both the 20160701\_control  
 681 and 20160701\_perturbed cases. This visualization provides a quantitative representation of the  
 682 change in CCN number concentration, which increases from a mean value of  $32.52 \text{ cm}^{-3}$  in the  
 683 control run to  $127.68 \text{ cm}^{-3}$  in the perturbed run, approximately four times higher than the control  
 684 run. Because we want to avoid counting high CCN number concentration above cloud top which  
 685 do not readily become cloud droplets, the CCN number concentration is averaged from the surface  
 686 up to the height of 1000 m (Wang et al., 2020).

687 The LWP in the 20160701\_control case exhibits a domain mean value of  $64.88 \text{ g m}^{-2}$ ,  
 688 which subsequently increases to  $123.27 \text{ g m}^{-2}$  in the 20160701\_perturbed case. As mentioned in  
 689 Section 3.1, the LWP for the 20160701 case follows a diurnal cycle, with higher values during  
 690 nighttime and lower values during daytime. This diurnal cycle is also observed in the perturbed  
 691 simulation, with the larger differences in CCN and LWP between the control run and perturbed  
 692 run during nighttime (Fig. 9a).

Deleted: under

Deleted: three

Deleted: are also hard to

Deleted: within

Deleted: height

698 After increasing ~~the aerosol concentration~~, the cloud droplet number in the  
699 20160701\_perturbed run demonstrates similar responses. In the 20160701\_control case, the  
700 domain mean value of ~~the~~ cloud droplet number is  $14.03 \text{ cm}^{-3}$ , which subsequently increases to  
701  $45.52 \text{ cm}^{-3}$  in the 20160701\_perturbed case. As the cloud droplet number increases, the cloud  
702 radius decreases from  $12.23 \text{ }\mu\text{m}$  in the control run to  $10.08 \text{ }\mu\text{m}$  in the perturbed case.

Deleted: aerosols

703 The case of 20170719 represents a post-trough weather regime, and Fig. 8c illustrates the  
704 passage of a frontal system in the area after ~~8 Z local time~~ on that day. In the 20170719\_perturbed  
705 simulation, the CWC increases following the system's passage (Fig. 8d) compared to the CWC in  
706 the 20170719\_control run. Additionally, the ambient CCN number in the perturbed run is also  
707 higher. The time variation of CCN concentration in Fig. 9c shows elevated CCN numbers before  
708 and after the system enters the domain. In the 20170719\_control case, the domain mean value of  
709 CCN number concentration is  $60.51 \text{ cm}^{-3}$ , which subsequently increases to  $253.51 \text{ cm}^{-3}$  in the  
710 20170719\_perturbed case. The domain-averaged LWP also exhibits an increase, rising from  $59.31$   
711  $\text{g m}^{-2}$  in the 20170719\_control run to  $74.07 \text{ g m}^{-2}$  in the 20170719\_perturbed case. Notably, this  
712 change primarily occurs after the passage of the frontal system.

Deleted: 9 UTC

713 The cloud droplet number consistently shows higher values in the perturbed case (Fig. 9d),  
714 and this pattern is similar to the difference in CCN between the two runs of 20170719 (Fig. 9c).  
715 In the 20170719\_control case, the domain mean value of cloud droplet number is  $20.70 \text{ cm}^{-3}$ , while  
716 the value is  $56.09 \text{ cm}^{-3}$  in the perturbed case. When the cloud droplet number increases in the  
717 perturbed run, the cloud radius decreases from  $9.90 \text{ }\mu\text{m}$  in the control run to  $7.49 \text{ }\mu\text{m}$  in the  
718 perturbed case. This reduction in cloud radius is even smaller than the cloud radius observed in  
719 the case of 20160701.

722 The case of 20190823 is similar to the case of 20170719, but it represents a weak trough  
 723 weather regime. Figure 8e also illustrates the passage of a cloud system in the area between 5 Z  
 724 to 17 Z local time on 23 August 2019, and the CWC in the perturbed run increases during this  
 725 period. Quantitatively, in the 20190823\_control case, the domain mean value of CCN number  
 726 concentration is  $124.32 \text{ cm}^{-3}$ , which subsequently increases to  $475.37 \text{ cm}^{-3}$  in the  
 727 20190823\_perturbed case, which is also about three times higher. The domain-averaged LWP  
 728 also exhibits an increase, rising from  $48.92 \text{ g m}^{-2}$  in the 20190823\_control run to  $58.53 \text{ g m}^{-2}$  in  
 729 the 20190823\_perturbed case.

730 Differing from the case of 20170719, the frontal system moved away from the study  
 731 domain after the noontime, the differences of CCN number or cloud droplet number between the  
 732 control and perturbed runs becomes even more pronounced after the system (Figs. 9e and 9f). It  
 733 is because aerosols are transported to the area following the frontal system (Fig. 4f) and then more  
 734 aerosols activated as CCN. In the 20190823\_control case, the domain mean value of cloud droplet  
 735 number is  $33.94 \text{ cm}^{-3}$ , while the value is  $79.97 \text{ cm}^{-3}$  in the perturbed case. When the cloud droplet  
 736 number increases in the perturbed run, the cloud radius decreases from  $8.51 \text{ }\mu\text{m}$  in the control run  
 737 to  $6.45 \text{ }\mu\text{m}$  in the perturbed case. This reduction in cloud radius is similar to the cloud radius  
 738 observed in the case of 20170719.

739 We observe that large aerosol-induced LWP occurs during the periods of rainfall (Fig. S9).  
 740 To accurately quantify the differences, we calculate the average LWP over approximately 25 km  
 741 of domain 4. This results in 16 averaged grids per output file, with each file generated every 10  
 742 minutes. This averaging process is based on Arola et al. (2022) and Zhou and Feingold (2023) to  
 743 avoid the impact of heterogeneity and co-variability on the results. Specifically, we aggregate the

Deleted: 6 UTC

Deleted: 18 UTC

Deleted: Differ

Deleted: 12 UTC

Deleted: S7

Deleted: the

750 simulation grids with a spacing resolution of approximately 190 m to form a larger grid of around  
751 25 km for each 10-minute simulation output, as shown in Fig. S10a.

Deleted: presented

Deleted: Table 2

752 Table 2 presents the 10-minute mean and standard deviation of several variables, including  
753 CCN, LWP, cloud droplet number (Nc), cloud radius (Re), and rainfall intensity (RI), across three  
754 study cases. The classification of "rain" and "non-rain" is based on the RI (unit: mm hr<sup>-1</sup>) on the  
755 averaged grid. Specifically, a grid is considered as "rain" if the RI is greater than zero. In the  
756 control cases, the averaged CCN number is 73.07 cm<sup>-3</sup>, and the corresponding LWP is 53.17 g m<sup>-2</sup>.  
757 However, in the perturbed cases, the CCN number increases approximately threefold, reaching  
758 218.21 cm<sup>-3</sup>, and the LWP increases by 49% to 79.25 g m<sup>-2</sup>. The introduction of additional aerosols  
759 in the perturbed cases also leads to a significant increase in the Nc number, from 22.68 cm<sup>-3</sup> in the  
760 control cases to 59.74 cm<sup>-3</sup> in the perturbed cases. Consequently, the Re decreases by 21% from  
761 9.97 μm to 7.83 μm, and the RI decreases by 11% from 0.009 mm hr<sup>-1</sup> to 0.008 mm hr<sup>-1</sup>.

762 To investigate the interaction between aerosols and clouds, we analyze the results  
763 separately for rain and non-rain grids. In both the control and perturbed cases, we observe that the  
764 CCN number within 1000 m is lower in the rain grids compared to the non-rain grids, primarily  
765 due to the washout effect caused by rainfall. Additionally, the LWP over the rain grids is generally  
766 higher than that over the non-rain grids. Furthermore, when comparing the control and perturbed  
767 cases, we find that the LWP over the rain grids increases by 57% from 58.57 g m<sup>-2</sup> to 91.81 g m<sup>-2</sup>.  
768 In contrast, the LWP over the non-rain grids only increases by 28% (Table 2). This difference can  
769 be attributed to the conversion of cloud droplets to raindrops through processes like autoconversion  
770 and collection, which occurs more prominently over the rain grids. We also observe that in the  
771 non-rain grids, especially at the cloud edges (or low LWP), the perturbed cases reveal an increased  
772 presence of small cloud droplets. This abundance of smaller droplets facilitates evaporation,

775 resulting in a reduced LWP (e.g., clouds in the bottom right corner of Figs. S10a and S10b).  
 776 Consequently,  $N_c$  over the rain grids is lower compared to  $N_c$  over the non-rain grids. Moreover,  
 777 when introducing aerosols in the perturbed runs, the results over the rain grids exhibit larger cloud  
 778 drops and a wider radius spectrum compared to the results over the non-rain grids. This suggests  
 779 that the presence of aerosols has a more pronounced effect on cloud properties within the rain  
 780 grids.

781 Zheng et al. (2022) conducted a study on the aerosol-cloud interaction using ground-based  
 782 measurements from the ARM program, focusing on the influence of environmental variables.  
 783 Their findings revealed that when there is ample water vapor and low CCN loading, the active  
 784 coalescence process leads to a broader size distribution of cloud droplets, resulting in an increase  
 785 in cloud droplet radius. On the other hand, when there is enhanced activation of CCN and  
 786 condensational growth of cloud droplets due to higher CCN loading below the cloud, the cloud  
 787 droplet radius decreases. This combined effect signifies an intensified aerosol-cloud interaction,  
 788 leading to a broad range of cloud droplet radii. The simulated results in our study, specifically  
 789 over the rain grids where a sufficient water vapor environment is considered, demonstrate a  
 790 significant aerosol-cloud interaction, where increased CCN introduces more newly converted  
 791 droplets, resulting in a broad range of cloud droplet radii.

792 Since we utilize a comprehensive aerosol module in WRF-Chem to examine aerosol-cloud  
 793 interactions, we are able to explore how changes in cloud properties, driven by increased CCN,  
 794 affect aerosol concentrations. For example, in the post-trough regime (20170917 case) and the  
 795 weak trough regime (20190823 case), we observe that the cloud structure exhibits more open-cell  
 796 stratocumulus clouds (Figs. 2h and 2i). As mentioned above, the increased number of smaller  
 797 cloud droplets at the cloud edge facilitate evaporation and results in a lower LWP (Fig. S10). The

Deleted: S8a

Deleted: S8b

Deleted: the

Deleted: number

Deleted: the

Deleted: number

Deleted: motioned

Deleted: S8



806 larger aerosols from the evaporated clouds return to the accumulation mode, making them more  
807 likely to activate as CCN again.

808 To demonstrate how robust this process on the ACI, we calculate the time series of the  
809 ratio of the ~~number concentration of CCN at a supersaturation of 0.2% in the perturbed runs to that~~  
810 ~~in the control runs, normalized by the corresponding accumulation mode aerosol concentration,~~  
811 defined as  $(CCN_{0.2\%}/Accu.aerosols)_{perturbed} / (CCN_{0.2\%}/Accu.aerosols)_{control}$ , shown in  
812 Fig. 10. A ratio greater than 1 suggests that accumulation mode aerosols in the perturbed cases  
813 are more readily activated as CCN at a supersaturation of 0.2%, especially in the cases of 20170719  
814 and 20190823. Conversely, a ratio less than 1 is observed during the first half of the day in the  
815 ~~20160701~~ case, which is attributed to the very low levels of accumulation mode aerosols in the  
816 model.

Deleted: percentage

Deleted: activated

Deleted: 0.2%

Deleted: to

Deleted: accumulation mode aerosols between

Deleted: and

Deleted: 20170701

### 817 3.4 Cloud liquid water path (LWP) susceptibilities

818 In this study, the susceptibility of LWP to changes in CCN concentration is quantified  
819 using the logarithmic slope between LWP and CCN, denoted as  $d\ln(LWP)/d\ln(CCN)$   
820 (Gryspeerd et al., 2019). This slope represents the sensitivity of ~~the LWP in~~ warm stratocumulus  
821 ~~clouds~~ to variations in CCN concentration, like shown in Fig. ~~S10c~~. As presented in Table 2, we  
822 aggregate the simulation grids with a spacing resolution of approximately 190 m to form a larger  
823 grid of around 25 km for each 10-minute simulation output. This averaging process helps to reduce  
824 the impact of heterogeneity and co-variability on the results.

Deleted: clouds' LWP

Deleted: S8c

825 Figure 11 illustrates the averaged cloud susceptibilities for various LWP and CCN or Nc  
826 bins across three study periods. The logarithmic slope between LWP and CCN is calculated at  
827 each output time (every 10 minutes) using data from 16 aggregated grid points from the control

run and 16 aggregated grid points from the perturbed run. Our study reveals that when the CCN concentration is below  $100 \text{ cm}^{-3}$ , the susceptibility for different LWP and CCN values is positive and the values are large, indicating that changes in LWP are sensitive to variations in CCN number. Here also demonstrates the AIE is large when an increase in CCN can have a large impact on LWP enhancement. However, when the mean CCN concentration exceeds  $100 \text{ cm}^{-3}$ , the relationship between LWP and CCN becomes more complex, with both positive and negative susceptibilities observed. This suggests that the change in LWP is influenced by other factors, such as environmental conditions and cloud precipitation status. (as shown in Fig. 11a). It is important to note that the CCN number used in our study is averaged from the surface up to the height of 1000 m, which may introduce uncertainty to the absolute values of susceptibility by including aerosols that are not directly involved in the aerosol-cloud interaction (Wang et al., 2020).

Additionally, our simulations indicate that the  $N_c$  in this study is generally low, with a mean value typically below  $80 \text{ cm}^{-3}$ . For different LWP and  $N_c$  values, the susceptibility is mostly positive, indicating that changes in LWP are sensitive to variations in  $N_c$  number (as shown in Fig. 11c).

When we investigate the variation of LWP susceptibility over time, we observe that positive susceptibilities for different LWP and CCN ( $N_c$ ) typically occur during periods of no rain or light rain (Figs. 12 and S9). On 1 July 2016, the time series of LWP susceptibility for different CCN or  $N_c$  shows a diurnal cycle, with large positive values during the nighttime and small positive values in the afternoon. During heavy rain events, such as from 8 to 15 Z local time on 19 July 2017 and from 23 Z to 14 Z on 23 August 2019 (Fig. S9), the LWP susceptibilities are negative or close to zero (Figs. 12c and 12e). In the perturbed cases, during the heavy rainfall periods, some aggregated grids show very low LWP (Fig. S10c). This reduction in LWP is caused

Deleted: susceptibility

Deleted: small,

Deleted: .

Deleted: not

Deleted: sensitive to changes in CCN number

Deleted: within a

Deleted: range

Deleted: S7

Deleted: 9

Deleted: 16 UTC

Deleted: 0

Deleted: 15 UTC

Deleted: S7

Deleted: S8c

874 by the evaporation from small cloud droplets at non-rain grids on the cloud edge. Those low LWP  
875 grids in the perturbed runs result in a negative or near-zero logarithmic slope between LWP and  
876 CCN (Figs. [S10c](#), 12c and 12e), although the domain mean LWP is higher in the perturbed case  
877 than in the control case (Figs. 9c and 9e).

Deleted: S8c

878 To further illustrate the reduction in LWP due to evaporation at the cloud edge, Fig. 13  
879 presents the relative change in  $\ln(LWP)$  between the perturbed and control cases across different  
880 LWP percentile ranges in the control case during the periods of negative LWP susceptibility, as  
881 shown in Fig. 12. The results indicate a decrease in LWP in the perturbed cases compared to the  
882 control cases for pixels with the lowest LWP percentile range (0-25%). We assume ~~that this range~~  
883 ~~corresponds to thin clouds~~ at the ~~edges of the cloud cover~~.

Deleted: %, which we

Deleted: occur

Deleted: edges

884 Figures 11b and 11d display the mean Re susceptibilities for different CCN ~~number~~ and  
885 Nc, respectively. The results consistently show that as CCN ~~number~~ or Nc increases, the radius  
886 of the cloud droplets decreases. Additionally, the change in Re is more pronounced when Nc (or  
887 CCN ~~number~~) is higher.

Deleted: the

888 In this study, the logarithmic slope between LWP and CCN in the LWP susceptibility  
889 calculation is based on a linear assumption. Hoffmann et al. (2024) introduced a heuristic model  
890 that represents a significant advancement in understanding the process-level adjustments of cloud  
891 water in stratocumulus clouds, suggesting that the relationship may resemble a reversed "V" shape.  
892 Figure 13 indicates that the decrease in LWP (negative susceptibilities) in the perturbed cases  
893 occurs only in low LWP clouds (thin and non-rain clouds). Conversely, LWP increases (positive  
894 susceptibilities) in thicker, precipitating clouds under the perturbed scenarios, which is consistent  
895 with the findings of Hoffmann et al. (2024). Since our study aggregates grids to a 25 km resolution,  
896 we are able to capture such spatial heterogeneity and retrieve a negative susceptibility due to the

evaporation of thin clouds at cloud edge while at 100-km scale (domain-averaged shown in Figs. S11 and S12), the signal is dominated by the increase of LWP at cloud core. However, based on the current study cases, we may not have sufficient data samples to illustrate a relationship beyond the linear assumption.

## 4 Discussion and summary

This study focuses on aerosol indirect effects (AIE), particularly involving long-range transport aerosols, in the Eastern North Atlantic (ENA) region. It specifically examines these effects on warm boundary layer stratiform clouds located on the eastern side of oceanic subtropical highs under three different weather regimes: a ridge with a surface high-pressure system, a post-trough with a surface high-pressure system, and a weak trough. We select three specific study cases (i.e., 20160701, 20170719, and 20190823) to assess the impact of long-range transport aerosols on warm boundary layer clouds, with each case representing a typical meteorological regime observed over the ENA site.

To investigate aerosol-cloud interactions more realistically, incorporating aerosol chemistry components that activate to cloud condensation nuclei (CCN) and accounting for aerosol spatiotemporal variation, this study employs the Weather Research and Forecast model coupled with a chemistry component (WRF-Chem). This approach provides a detailed examination of AIE in the ENA region under the three specified weather regimes. We employ a downscaling technique to conduct WRF-Chem simulations for the two inner domains (with the outer domains utilizing WRF). This approach results in nearly a 50% reduction in total computational costs, achieving a throughput of 8 hours per day using 1,080 cores.

We incorporate major aerosol species (BC, OC, and SO<sub>4</sub>), as well as SO<sub>2</sub>, from MERRA-2 to provide aerosol initial and boundary conditions, labeled as control cases. Additionally, we

925 formulate three perturbed cases by amplifying aerosol concentrations in both initial and boundary  
926 conditions, as well as sea salt emissions, by a factor of five relative to each control case. Since  
927 aerosol features are primarily determined by aerosol initial and boundary conditions, a higher  
928 Aiken mode assumption in the major aerosol component (i.e., SO<sub>4</sub>) regarding the aerosol mode  
929 ratio (80% for Aiken mode and 20% for accumulation mode) results in fewer aerosols activating  
930 as CCN due to the curvature effect in our simulations.

931 The WRF-Chem model captures the cloud structure in the case of 20160701, ~~but~~  
932 ~~underestimates the cloud amount.~~ It simulates the formation of thin, uniform stratocumulus clouds  
933 within a meteorological regime characterized by a ridge system in the free troposphere and a high-  
934 pressure system near the surface. However, the cases of 20170719 and 20190823 exhibit the  
935 development of ~~thicker but broken~~ solid stratocumulus clouds within a post-trough regime and a  
936 weak trough, respectively. With the fast-moving cloud systems and strong surface wind, the WRF-  
937 Chem model ~~struggles~~ to capture the development and movement of these cloud systems due to  
938 delayed moisture transport from outer boundary condition and potential insufficient vertical  
939 resolution.

940 In all cases, compared to the observations, the WRF-Chem model underestimates the liquid  
941 water path (LWP) and cloud fraction due to warmer and lower simulated boundary layer. In the  
942 perturbed cases, we find 57% higher aerosol-induced LWP, especially ~~for the rain grids.~~ We also  
943 note that the perturbed cases exhibit lower rainfall intensity, indicating a rainfall suppression effect  
944 attributed to high CCN concentrations as concluded in previous studies (Wang et al., 2020;  
945 Christensen et al., 2024). In contrast, the LWP over the non-rain grids only increases by 28%.  
946 Moreover, when introducing aerosols in the perturbed runs, the results over the rain grids exhibit  
947 larger cloud drops and a wider radius spectrum compared to the results over the non-rain grids.

Deleted: .

Deleted: broke and

Deleted: struggle

Deleted: during

Deleted: periods of rainfall

953 This suggests that the presence of aerosols has a more pronounced effect on cloud properties within  
954 the rain grids. The non-rain grids over the cloud edge can have lower LWP because smaller cloud  
955 droplets are easy to evaporate.

956 Our study further elucidates the intricate feedback mechanisms governing aerosol-cloud  
957 interactions and aerosol properties. In both the post-trough and weak trough regimes, we observe  
958 a pronounced tendency for the cloud structure to develop more open-cell stratocumulus clouds.  
959 At the peripheries of these clouds, the perturbed cases demonstrate a significant increase in the  
960 presence of small cloud droplets. This heightened abundance of smaller droplets promotes  
961 evaporation, thereby leading to a marked reduction in LWP.

Deleted: not only

Deleted: but also leads

962 As these clouds evaporate, the aerosols that are released return to the accumulation mode.  
963 This transition enhances their likelihood of reactivating as CCN. Consequently, this cycle  
964 underscores the dynamic interplay between aerosol properties and cloud formation, highlighting  
965 how changes in aerosol concentrations can influence cloud microphysics and, ultimately,  
966 precipitation processes.

Deleted: larger

967 Additionally, the susceptibility of LWP to changes in CCN concentration is quantified  
968 using the logarithmic slope between LWP and CCN. Our result shows when the CCN  
969 concentration is low, LWP is sensitive to variations in CCN number, with higher CCN number  
970 concentration leading to higher LWP. However, when the mean CCN concentration is relatively  
971 high, LWP is not as sensitive to changes in CCN, the LWP susceptibilities are small in magnitude,  
972 with both positive and negative values. Those negative values are caused by the evaporation from  
973 small cloud droplets at non-rain grids on the cloud edge.

974 In Wang et al. (2020), the LWC susceptibility for a light precipitation case on 18 July 2017  
975 also shows positive values based on three sensitivity runs with CCN concentrations of 10, 100,

979 and  $1000 \text{ cm}^{-3}$ . The cloud properties in their study are averaged over all cloud points in the  
 980 innermost domain. We adopt the same method as Wang et al. (2020) to estimate the LWP  
 981 susceptibility using the domain mean values, defined as  
 982  $\Delta \ln(LWP_{perturbed} - LWP_{control}) / \Delta \ln(CCN_{perturbed} - CCN_{control})$ . This approach  
 983 predominantly yields positive values for LWP susceptibility across the three study cases (see Figs.

984 S11 and S12). This suggests that the 25-km resolution is able to capture such spatial heterogeneity  
 985 and retrieve a negative susceptibility due to the evaporation of thin clouds at cloud edge while at  
 986 100-km scale (domain-averaged), the signal is dominated by the increase of LWP at cloud core.

987 Conversely, the LWP susceptibilities associated with varying cloud droplet numbers  
 988 reported in Qiu et al. (2024) reveal significant negative values in LWP susceptibility in response  
 989 to high cloud droplet numbers, a trend that is partially reflected in our study. Further investigation  
 990 is required to reconcile the difference in LWP responses between observational data and model  
 991 simulations. Additionally, a more accurate estimation of LWP susceptibility to changes in CCN  
 992 concentration is necessary.

993 Moreover, future research will focus on addressing the identified issues within the model,  
 994 such as improving the representation of transported aerosol size distributions, resolving the overly  
 995 fragmented stratocumulus cloud layers with sharp boundary layer inversions, and comparing the  
 996 modeled cloud susceptibilities with observational data through simulations of ship tracks and local  
 997 aerosol perturbations.

998

999 **Code and data availability:**

Deleted: S9

Deleted: S10

Deleted: critical for accurately estimating LWP

Deleted: . A resolution that is too coarse (i.e., using

Deleted: mean) may fail to capture finer details, such as

Deleted: aerosol drying effects occurring

Deleted: the

Deleted: edges

1008 The WRF-Chem code (v4.4.2) used in this study has been released on GitHub  
1009 (<https://github.com/wrf-model/WRF/releases/download/v4.4.2/v4.4.2.tar.gz>). The observational  
1010 data used in this study are available at <https://doi.org/10.5281/zenodo.13356995>. Other WRF-  
1011 Chem simulated outputs for the plots in this paper are available at  
1012 <https://doi.org/10.5281/zenodo.13357040>.

1013

#### 1014 **Author contributions:**

1015 H.-H. Lee and X. Zheng provided ideas and designed the experiments in this study. H.-H. Lee  
1016 conducted all the simulations and analyses. H.-H. Lee leads and coordinates the manuscript with  
1017 inputs from coauthors.

1018

#### 1019 **Competing interests.**

1020 At least one of the (co-)authors is a member of the editorial board of Atmospheric Chemistry and  
1021 Physics.

1022

#### 1023 **Acknowledgements:**

1024 This work is supported by the DOE Office of Science Early Career Research Program and the  
1025 ASR Program. Work at LLNL was performed under the auspices of the U.S. DOE by Lawrence  
1026 Livermore National Laboratory under contract DE-AC52-07NA27344. LLNL IM: LLNL-JRNL-

1027 870513.

1028

Deleted: -DRAFT



## 1030 **Reference:**

- 1031 Abdul-Razzak, H. and Ghan, S. J.: A parameterization of aerosol activation: 2. Multiple  
 1032 aerosol types, *Journal of Geophysical Research: Atmospheres*, 105, 6837-6844,  
 1033 <https://doi.org/10.1029/1999JD901161>, 2000.
- 1034 Ackermann, I. J., Hass, H., Memmesheimer, M., Ebel, A., Binkowski, F. S., and Shankar, U.:  
 1035 Modal aerosol dynamics model for Europe: development and first applications,  
 1036 *Atmospheric Environment*, 32, 2981-2999, [http://dx.doi.org/10.1016/S1352-](http://dx.doi.org/10.1016/S1352-2310(98)00006-5)  
 1037 [2310\(98\)00006-5](http://dx.doi.org/10.1016/S1352-2310(98)00006-5), 1998.
- 1038 Albrecht, B. A.: Aerosols, Cloud Microphysics, and Fractional Cloudiness, *Science*, 245,  
 1039 1227-1230, doi:10.1126/science.245.4923.1227, 1989.
- 1040 Arola, A., Lipponen, A., Kolmonen, P., Virtanen, T. H., Bellouin, N., Grosvenor, D. P.,  
 1041 Gryspeerdt, E., Quaas, J., and Kokkola, H.: Aerosol effects on clouds are concealed by  
 1042 natural cloud heterogeneity and satellite retrieval errors, *Nature Communications*, 13,  
 1043 7357, 10.1038/s41467-022-34948-5, 2022.
- 1044 Binkowski, F. S. and Shankar, U.: The Regional Particulate Matter Model: 1. Model  
 1045 description and preliminary results, *Journal of Geophysical Research: Atmospheres*, 100,  
 1046 26191-26209, <https://doi.org/10.1029/95JD02093>, 1995.
- 1047 Cadeddu, M. P., Ghate, V. P., and Mech, M.: Ground-based observations of cloud and  
 1048 drizzle liquid water path in stratocumulus clouds, *Atmos. Meas. Tech.*, 13, 1485-1499,  
 1049 10.5194/amt-13-1485-2020, 2020.
- 1050 Chapman, E. G., Gustafson Jr, W. I., Easter, R. C., Barnard, J. C., Ghan, S. J., Pekour, M. S.,  
 1051 and Fast, J. D.: Coupling aerosol-cloud-radiative processes in the WRF-Chem model:  
 1052 Investigating the radiative impact of elevated point sources, *Atmos. Chem. Phys.*, 9, 945-  
 1053 964, 10.5194/acp-9-945-2009, 2009.
- 1054 Chen, F. and Dudhia, J.: Coupling an Advanced Land Surface-Hydrology Model with the  
 1055 Penn State-NCAR MM5 Modeling System. Part I: Model Implementation and Sensitivity,  
 1056 *Monthly Weather Review*, 129, 569-585, [https://doi.org/10.1175/1520-](https://doi.org/10.1175/1520-0493(2001)129<0569:CAALSH>2.0.CO;2)  
 1057 [0493\(2001\)129<0569:CAALSH>2.0.CO;2](https://doi.org/10.1175/1520-0493(2001)129<0569:CAALSH>2.0.CO;2), 2001.
- 1058 Chen, T., Rossow, W. B., and Zhang, Y.: Radiative Effects of Cloud-Type Variations, *Journal*  
 1059 *of Climate*, 13, 264-286, 10.1175/1520-0442(2000)013<0264:Reoctv>2.0.Co;2, 2000.
- 1060 Chin, M., Ginoux, P., Kinne, S., Torres, O., Holben, B. N., Duncan, B. N., Martin, R. V.,  
 1061 Logan, J. A., Higurashi, A., and Nakajima, T.: Tropospheric Aerosol Optical Thickness from  
 1062 the GOCART Model and Comparisons with Satellite and Sun Photometer Measurements,  
 1063 *Journal of the Atmospheric Sciences*, 59, 461-483, [https://doi.org/10.1175/1520-](https://doi.org/10.1175/1520-0469(2002)059<0461:TAOTFT>2.0.CO;2)  
 1064 [0469\(2002\)059<0461:TAOTFT>2.0.CO;2](https://doi.org/10.1175/1520-0469(2002)059<0461:TAOTFT>2.0.CO;2), 2002.
- 1065 Christensen, M. W., Wu, P., Varble, A. C., Xiao, H., and Fast, J. D.: Aerosol-induced closure  
 1066 of marine cloud cells: enhanced effects in the presence of precipitation, *Atmos. Chem.*  
 1067 *Phys.*, 24, 6455-6476, 10.5194/acp-24-6455-2024, 2024.
- 1068 Clarke, A. D., Owens, S. R., and Zhou, J.: An ultrafine sea-salt flux from breaking waves:  
 1069 Implications for cloud condensation nuclei in the remote marine atmosphere, *Journal of*  
 1070 *Geophysical Research: Atmospheres*, 111, <https://doi.org/10.1029/2005JD006565>, 2006.

1071 Fast, J. D., Gustafson Jr., W. I., Easter, R. C., Zaveri, R. A., Barnard, J. C., Chapman, E. G.,  
 1072 Grell, G. A., and Peckham, S. E.: Evolution of ozone, particulates, and aerosol direct  
 1073 radiative forcing in the vicinity of Houston using a fully coupled meteorology-chemistry-  
 1074 aerosol model, *Journal of Geophysical Research: Atmospheres*, 111,  
 1075 <https://doi.org/10.1029/2005JD006721>, 2006.  
 1076 Feingold, G., Ghate, V. P., Russell, L. M., Blossey, P., Cantrell, W., Christensen, M. W.,  
 1077 Diamond, M. S., Gettelman, A., Glassmeier, F., Gryspeerdt, E., Haywood, J., Hoffmann, F.,  
 1078 Kaul, C. M., Lebsock, M., McComiskey, A. C., McCoy, D. T., Ming, Y., Mülmenstädt, J.,  
 1079 Possner, A., Prabhakaran, P., Quinn, P. K., Schmidt, K. S., Shaw, R. A., Singer, C. E.,  
 1080 Sorooshian, A., Toll, V., Wan, J. S., Wood, R., Yang, F., Zhang, J., and Zheng, X.: Physical  
 1081 science research needed to evaluate the viability and risks of marine cloud brightening,  
 1082 *Science Advances*, 10, eadi8594, doi:10.1126/sciadv.adi8594, 2024.  
 1083 Gallo, F., Uin, J., Sanchez, K. J., Moore, R. H., Wang, J., Wood, R., Mei, F., Flynn, C.,  
 1084 Springston, S., Azevedo, E. B., Kuang, C., and Aiken, A. C.: Long-range transported  
 1085 continental aerosol in the eastern North Atlantic: three multiday event regimes influence  
 1086 cloud condensation nuclei, *Atmos. Chem. Phys.*, 23, 4221-4246, 10.5194/acp-23-4221-  
 1087 2023, 2023.  
 1088 Ghate, V. P. and Cadeddu, M. P.: Drizzle and Turbulence Below Closed Cellular Marine  
 1089 Stratocumulus Clouds, *Journal of Geophysical Research: Atmospheres*, 124, 5724-5737,  
 1090 <https://doi.org/10.1029/2018JD030141>, 2019.  
 1091 Ghate, V. P., Surlita, T., Magaritz-Ronen, L., Raveh-Rubin, S., Gallo, F., Carlton, A. G., and  
 1092 Azevedo, E. B.: Drivers of Cloud Condensation Nuclei in the Eastern North Atlantic as  
 1093 Observed at the ARM Site, *Journal of Geophysical Research: Atmospheres*, 128,  
 1094 e2023JD038636, <https://doi.org/10.1029/2023JD038636>, 2023.  
 1095 Gong, S. L.: A parameterization of sea-salt aerosol source function for sub- and super-  
 1096 micron particles, *Global Biogeochemical Cycles*, 17,  
 1097 <https://doi.org/10.1029/2003GB002079>, 2003.  
 1098 Grell, G. A., Peckham, S. E., Schmitz, R., McKeen, S. A., Frost, G., Skamarock, W. C., and  
 1099 Eder, B.: Fully coupled “online” chemistry within the WRF model, *Atmospheric*  
 1100 *Environment*, 39, 6957-6975, <https://doi.org/10.1016/j.atmosenv.2005.04.027>, 2005.  
 1101 Gryspeerdt, E., Goren, T., Sourdeval, O., Quaas, J., Mülmenstädt, J., Dipu, S., Unglaub, C.,  
 1102 Gettelman, A., and Christensen, M.: Constraining the aerosol influence on cloud liquid  
 1103 water path, *Atmos. Chem. Phys.*, 19, 5331-5347, 10.5194/acp-19-5331-2019, 2019.  
 1104 Hartmann, D. L., Ockert-Bell, M. E., and Michelsen, M. L.: The Effect of Cloud Type on  
 1105 Earth's Energy Balance: Global Analysis, *Journal of Climate*, 5, 1281-1304, 10.1175/1520-  
 1106 0442(1992)005<1281:Teocto>2.0.Co;2, 1992.  
 1107 Hersbach, H., Bell, B., Berrisford, P., Biavati, G., Horányi, A., Muñoz Sabater, J., Nicolas, J.,  
 1108 Peubey, C., Radu, R., Rozum, I., Schepers, D., Simmons, A., Soci, C., Dee, D., and Thépaut,  
 1109 J.-N.: ERA5 hourly data on single levels from 1940 to present. Copernicus Climate Change  
 1110 Service (C3S) Climate Data Store (CDS) [dataset], 10.24381/cds.adbb2d47 2023.  
 1111 [Hoffmann, F., Glassmeier, F., and Feingold, G.: The impact of aerosol on cloud water: a](https://doi.org/10.24381/cds.adbb2d47)  
 1112 [heuristic perspective, \*Atmos. Chem. Phys.\*, 24, 13403-13412, 10.5194/acp-24-13403-](https://doi.org/10.5194/acp-24-13403-2024)  
 1113 [2024, 2024.](https://doi.org/10.5194/acp-24-13403-2024)

1114 Hong, S.-Y. and Jang, J.: Impacts of Shallow Convection Processes on a Simulated Boreal  
 1115 Summer Climatology in a Global Atmospheric Model, *Asia-Pacific Journal of Atmospheric*  
 1116 *Sciences*, 54, 361-370, 10.1007/s13143-018-0013-3, 2018.  
 1117 Iacono, M. J., Delamere, J. S., Mlawer, E. J., Shephard, M. W., Clough, S. A., and Collins, W.  
 1118 D.: Radiative forcing by long-lived greenhouse gases: Calculations with the AER radiative  
 1119 transfer models, *Journal of Geophysical Research: Atmospheres*, 113,  
 1120 10.1029/2008jd009944, 2008.  
 1121 Janjić, Z. I.: The Step-Mountain Eta Coordinate Model: Further Developments of the  
 1122 Convection, Viscous Sublayer, and Turbulence Closure Schemes, *Monthly Weather*  
 1123 *Review*, 122, 927-945, [https://doi.org/10.1175/1520-](https://doi.org/10.1175/1520-0493(1994)122<0927:TSMECM>2.0.CO;2)  
 1124 [0493\(1994\)122<0927:TSMECM>2.0.CO;2](https://doi.org/10.1175/1520-0493(1994)122<0927:TSMECM>2.0.CO;2), 1994.  
 1125 Kazemirad, M. and Miller, M. A.: Summertime Post-Cold-Frontal Marine Stratocumulus  
 1126 Transition Processes over the Eastern North Atlantic, *Journal of the Atmospheric Sciences*,  
 1127 77, 2011-2037, <https://doi.org/10.1175/JAS-D-19-0167.1>, 2020.  
 1128 Kazil, J., Wang, H., Feingold, G., Clarke, A. D., Snider, J. R., and Bandy, A. R.: Modeling  
 1129 chemical and aerosol processes in the transition from closed to open cells during  
 1130 VOCALS-REx, *Atmos. Chem. Phys.*, 11, 7491-7514, 10.5194/acp-11-7491-2011, 2011.  
 1131 Klein, S. A. and Hartmann, D. L.: The Seasonal Cycle of Low Stratiform Clouds, *Journal of*  
 1132 *Climate*, 6, 1587-1606, 10.1175/1520-0442(1993)006<1587:Tscols>2.0.Co;2, 1993.  
 1133 Knierel, J. C., Bryan, G. H., and Hacker, J. P.: Explicit Numerical Diffusion in the WRF  
 1134 Model, *Monthly Weather Review*, 135, 3808-3824,  
 1135 <https://doi.org/10.1175/2007MWR2100.1>, 2007.  
 1136 Lee, S. S., Donner, L. J., Phillips, V. T. J., and Ming, Y.: The dependence of aerosol effects on  
 1137 clouds and precipitation on cloud-system organization, shear and stability, *Journal of*  
 1138 *Geophysical Research: Atmospheres*, 113, <https://doi.org/10.1029/2007JD009224>, 2008.  
 1139 Liljegren, J. C., Clothiaux, E. E., Mace, G. G., Kato, S., and Dong, X.: A new retrieval for  
 1140 cloud liquid water path using a ground-based microwave radiometer and measurements of  
 1141 cloud temperature, *Journal of Geophysical Research: Atmospheres*, 106, 14485-14500,  
 1142 <https://doi.org/10.1029/2000JD900817>, 2001.  
 1143 Liu, X., Easter, R. C., Ghan, S. J., Zaveri, R., Rasch, P., Shi, X., Lamarque, J. F., Gettelman,  
 1144 A., Morrison, H., Vitt, F., Conley, A., Park, S., Neale, R., Hannay, C., Ekman, A. M. L., Hess,  
 1145 P., Mahowald, N., Collins, W., Iacono, M. J., Bretherton, C. S., Flanner, M. G., and Mitchell,  
 1146 D.: Toward a minimal representation of aerosols in climate models: description and  
 1147 evaluation in the Community Atmosphere Model CAM5, *Geosci. Model Dev.*, 5, 709-739,  
 1148 10.5194/gmd-5-709-2012, 2012.  
 1149 Logan, T., Xi, B., and Dong, X.: Aerosol properties and their influences on marine boundary  
 1150 layer cloud condensation nuclei at the ARM mobile facility over the Azores, *Journal of*  
 1151 *Geophysical Research: Atmospheres*, 119, 4859-4872,  
 1152 <https://doi.org/10.1002/2013JD021288>, 2014.  
 1153 Mather, J. H. and Voyles, J. W.: The Arm Climate Research Facility: A Review of Structure  
 1154 and Capabilities, *Bulletin of the American Meteorological Society*, 94, 377-392,  
 1155 <https://doi.org/10.1175/BAMS-D-11-00218.1>, 2013.  
 1156 McCoy, I. L., Wyant, M. C., Blossey, P. N., Bretherton, C. S., and Wood, R.: Aitken Mode  
 1157 Aerosols Buffer Decoupled Mid-Latitude Boundary Layer Clouds Against Precipitation

1158 Depletion, *Journal of Geophysical Research: Atmospheres*, 129, e2023JD039572,  
1159 <https://doi.org/10.1029/2023JD039572>, 2024.

1160 Mecham, D. B., Wittman, C. S., Miller, M. A., Yuter, S. E., and de Szoeke, S. P.: Joint  
1161 Synoptic and Cloud Variability over the Northeast Atlantic near the Azores, *Journal of*  
1162 *Applied Meteorology and Climatology*, 57, 1273-1290, [https://doi.org/10.1175/JAMC-D-17-](https://doi.org/10.1175/JAMC-D-17-0211.1)  
1163 [0211.1](https://doi.org/10.1175/JAMC-D-17-0211.1), 2018.

1164 Mellor, G. L. and Yamada, T.: Development of a turbulence closure model for geophysical  
1165 fluid problems, *Reviews of Geophysics*, 20, 851-875,  
1166 <https://doi.org/10.1029/RG020i004p00851>, 1982.

1167 Minnis, P., Sun-Mack, S., Young, D. F., Heck, P. W., Garber, D. P., Chen, Y., Spangenberg,  
1168 D. A., Arduini, R. F., Trepte, Q. Z., Smith, W. L., Ayers, J. K., Gibson, S. C., Miller, W. F.,  
1169 Hong, G., Chakrapani, V., Takano, Y., Liou, K. N., Xie, Y., and Yang, P.: CERES Edition-2  
1170 Cloud Property Retrievals Using TRMM VIRS and Terra and Aqua MODIS Data—Part I:  
1171 Algorithms, *IEEE Transactions on Geoscience and Remote Sensing*, 49, 4374-4400,  
1172 10.1109/TGRS.2011.2144601, 2011.

1173 Minnis, P., Sun-Mack, S., Chen, Y., Chang, F. L., Yost, C. R., Smith, W. L., Heck, P. W.,  
1174 Arduini, R. F., Bedka, S. T., Yi, Y., Hong, G., Jin, Z., Painemal, D., Palikonda, R., Scarino, B.  
1175 R., Spangenberg, D. A., Smith, R. A., Trepte, Q. Z., Yang, P., and Xie, Y.: CERES MODIS  
1176 Cloud Product Retrievals for Edition 4—Part I: Algorithm Changes, *IEEE Transactions on*  
1177 *Geoscience and Remote Sensing*, 59, 2744-2780, 10.1109/TGRS.2020.3008866, 2021.

1178 Mlawer, E. J., Taubman, S. J., Brown, P. D., Iacono, M. J., and Clough, S. A.: Radiative  
1179 transfer for inhomogeneous atmospheres: RRTM, a validated correlated-k model for the  
1180 longwave, *Journal of Geophysical Research: Atmospheres*, 102, 16663-16682,  
1181 <https://doi.org/10.1029/97JD00237>, 1997.

1182 Modeling, G. and Office, A.: MERRA-2 inst3\_3d\_aer\_Nv: 3d, 3-hourly, instantaneous,  
1183 model-level, assimilation, aerosol mixing ratio V5. 12.4, 2015.

1184 Molod, A., Takacs, L., Suarez, M., and Bacmeister, J.: Development of the GEOS-5  
1185 atmospheric general circulation model: evolution from MERRA to MERRA2, *Geosci. Model*  
1186 *Dev.*, 8, 1339-1356, 10.5194/gmd-8-1339-2015, 2015.

1187 Monin, A. S. and Obukhov, A. M.: Basic laws of turbulent mixing in the atmosphere near the  
1188 ground, *Tr. Inst. Teor. Geofiz. Akad. Nauk SSSR*, 24, 1963-1987, 1954.

1189 Morrison, H., Thompson, G., and Tatarskii, V.: Impact of Cloud Microphysics on the  
1190 Development of Trailing Stratiform Precipitation in a Simulated Squall Line: Comparison of  
1191 One- and Two-Moment Schemes, *Monthly Weather Review*, 137, 991-1007,  
1192 <https://doi.org/10.1175/2008MWR2556.1>, 2009.

1193 Painemal, D., Spangenberg, D., Smith Jr, W. L., Minnis, P., Cairns, B., Moore, R. H.,  
1194 Crosbie, E., Robinson, C., Thornhill, K. L., Winstead, E. L., and Ziemba, L.: Evaluation of  
1195 satellite retrievals of liquid clouds from the GOES-13 imager and MODIS over the  
1196 midlatitude North Atlantic during the NAAMES campaign, *Atmos. Meas. Tech.*, 14, 6633-  
1197 6646, 10.5194/amt-14-6633-2021, 2021.

1198 Qiu, S., Zheng, X., Painemal, D., Terai, C. R., and Zhou, X.: Daytime variation in the aerosol  
1199 indirect effect for warm marine boundary layer clouds in the eastern North Atlantic, *Atmos.*  
1200 *Chem. Phys.*, 24, 2913-2935, 10.5194/acp-24-2913-2024, 2024.

1201 Rémillard, J. and Tselioudis, G.: Cloud Regime Variability over the Azores and Its  
 1202 Application to Climate Model Evaluation, *Journal of Climate*, 28, 9707-9720,  
 1203 <https://doi.org/10.1175/JCLI-D-15-0066.1>, 2015.  
 1204 Schell, B., Ackermann, I. J., Hass, H., Binkowski, F. S., and Ebel, A.: Modeling the formation  
 1205 of secondary organic aerosol within a comprehensive air quality model system, *Journal of*  
 1206 *Geophysical Research: Atmospheres* (1984–2012), 106, 28275-28293, 2001.  
 1207 Skamarock, W., Klemp, J., Dudhia, J., Gill, D., Liu, Z., Berner, J., and Huang, X.: A  
 1208 description of the advanced research WRF model version 4.3 (No. NCAR/TN-556+  
 1209 STR).[Software], 2021.  
 1210 Skamarock, W. C., Klemp, J. B., Dudhia, J., Gill, D. O., Barker, D. M., Duda, M. G., Huang,  
 1211 X.-Y., Wang, W., and Powers, J. G.: A description of the advanced research WRF version 3,  
 1212 NCAR technical note, 475, 10.5065, 2008.  
 1213 Stephens, G. L. and Greenwald, T. J.: The Earth's radiation budget and its relation to  
 1214 atmospheric hydrology: 2. Observations of cloud effects, *Journal of Geophysical Research:*  
 1215 *Atmospheres*, 96, 15325-15340, 10.1029/91jd00972, 1991.  
 1216 Stockwell, W. R., Kirchner, F., Kuhn, M., and Seefeld, S.: A new mechanism for regional  
 1217 atmospheric chemistry modeling, *Journal of Geophysical Research: Atmospheres*, 102,  
 1218 25847-25879, 10.1029/97JD00849, 1997.  
 1219 [Terai, C. R., Bretherton, C. S., Wood, R., and Painter, G.: Aircraft observations of aerosol,](#)  
 1220 [cloud, precipitation, and boundary layer properties in pockets of open cells over the](#)  
 1221 [southeast Pacific, \*Atmos. Chem. Phys.\*, 14, 8071-8088, 10.5194/acp-14-8071-2014, 2014.](#)  
 1222 Tian, J., Dong, X., Xi, B., Williams, C. R., and Wu, P.: Estimation of liquid water path below  
 1223 the melting layer in stratiform precipitation systems using radar measurements during  
 1224 MC3E, *Atmos. Meas. Tech.*, 12, 3743-3759, 10.5194/amt-12-3743-2019, 2019.  
 1225 Toon, O. B., Kasting, J. F., Turco, R. P., and Liu, M. S.: The sulfur cycle in the marine  
 1226 atmosphere, *Journal of Geophysical Research: Atmospheres*, 92, 943-963,  
 1227 <https://doi.org/10.1029/JD092iD01p00943>, 1987.  
 1228 Tuccella, P., Curci, G., Visconti, G., Bessagnet, B., Menut, L., and Park, R. J.: Modeling of  
 1229 gas and aerosol with WRF/Chem over Europe: Evaluation and sensitivity study, *Journal of*  
 1230 *Geophysical Research: Atmospheres*, 117, <https://doi.org/10.1029/2011JD016302>, 2012.  
 1231 Twomey, S.: Pollution and the planetary albedo, *Atmospheric Environment* (1967), 8, 1251-  
 1232 1256, [https://doi.org/10.1016/0004-6981\(74\)90004-3](https://doi.org/10.1016/0004-6981(74)90004-3), 1974.  
 1233 Twomey, S.: Aerosols, clouds and radiation, *Atmospheric Environment. Part A. General*  
 1234 *Topics*, 25, 2435-2442, [https://doi.org/10.1016/0960-1686\(91\)90159-5](https://doi.org/10.1016/0960-1686(91)90159-5), 1991.  
 1235 Wang, J., Wood, R., Jensen, M. P., Chiu, J. C., Liu, Y., Lamer, K., Desai, N., Giangrande, S.  
 1236 E., Knopf, D. A., Kollias, P., Laskin, A., Liu, X., Lu, C., Mechem, D., Mei, F., Starzec, M.,  
 1237 Tomlinson, J., Wang, Y., Yum, S. S., Zheng, G., Aiken, A. C., Azevedo, E. B., Blanchard, Y.,  
 1238 China, S., Dong, X., Gallo, F., Gao, S., Ghate, V. P., Glienke, S., Goldberger, L., Hardin, J. C.,  
 1239 Kuang, C., Luke, E. P., Matthews, A. A., Miller, M. A., Moffet, R., Pekour, M., Schmid, B.,  
 1240 Sedlacek, A. J., Shaw, R. A., Shilling, J. E., Sullivan, A., Suski, K., Veghte, D. P., Weber, R.,  
 1241 Wyant, M., Yeom, J., Zawadowicz, M., and Zhang, Z.: Aerosol and Cloud Experiments in the  
 1242 Eastern North Atlantic (ACE-ENA), *Bulletin of the American Meteorological Society*, 103,  
 1243 E619-E641, <https://doi.org/10.1175/BAMS-D-19-0220.1>, 2022.

1244 Wang, Y., Zheng, X., Dong, X., Xi, B., Wu, P., Logan, T., and Yung, Y. L.: Impacts of long-  
 1245 range transport of aerosols on marine-boundary-layer clouds in the eastern North Atlantic,  
 1246 Atmos. Chem. Phys., 20, 14741-14755, 10.5194/acp-20-14741-2020, 2020.  
 1247 Warren, S. G., Hahn, C. J., London, J., Chervin, R. M., Jenne, R. L., Colorado Univ., B., CO .  
 1248 Cooperative Inst. for Research in Environmental Sciences, Colorado Univ., B., CO . Dept.  
 1249 of Astrophysical, Planetary,, Sciences, A., and National Center for Atmospheric Research,  
 1250 B., CO ): Global distribution of total cloud cover and cloud type amounts over the ocean,  
 1251 United States, Medium: ED; Size: Pages: (305 p), 10.2172/5415329, 1988.  
 1252 Wood, R.: Stratocumulus Clouds, Monthly Weather Review, 140, 2373-2423,  
 1253 10.1175/mwr-d-11-00121.1, 2012.  
 1254 Wood, R., Wyant, M., Bretherton, C. S., Rémillard, J., Kollias, P., Fletcher, J., Stemmler, J.,  
 1255 de Szoeke, S., Yuter, S., Miller, M., Mechem, D., Tselioudis, G., Chiu, J. C., Mann, J. A. L.,  
 1256 O'Connor, E. J., Hogan, R. J., Dong, X., Miller, M., Ghate, V., Jefferson, A., Min, Q., Minnis,  
 1257 P., Palikonda, R., Albrecht, B., Luke, E., Hannay, C., and Lin, Y.: Clouds, Aerosols, and  
 1258 Precipitation in the Marine Boundary Layer: An Arm Mobile Facility Deployment, Bulletin of  
 1259 the American Meteorological Society, 96, 419-440, [https://doi.org/10.1175/BAMS-D-13-](https://doi.org/10.1175/BAMS-D-13-00180.1)  
 1260 [00180.1](https://doi.org/10.1175/BAMS-D-13-00180.1), 2015.  
 1261 Zaveri, R. A., Barnard, J. C., Easter, R. C., Riemer, N., and West, M.: Particle-resolved  
 1262 simulation of aerosol size, composition, mixing state, and the associated optical and cloud  
 1263 condensation nuclei activation properties in an evolving urban plume, Journal of  
 1264 Geophysical Research: Atmospheres, 115, <https://doi.org/10.1029/2009JD013616>, 2010.  
 1265 Zhang, H., DeNero, S. P., Joe, D. K., Lee, H. H., Chen, S. H., Michalakes, J., and Kleeman,  
 1266 M. J.: Development of a source oriented version of the WRF/Chem model and its  
 1267 application to the California regional PM<sub>10</sub> / PM<sub>2.5</sub> air quality  
 1268 study, Atmos. Chem. Phys., 14, 485-503, 10.5194/acp-14-485-2014, 2014.  
 1269 Zhang, Z., Song, Q., Mechem, D. B., Larson, V. E., Wang, J., Liu, Y., Witte, M. K., Dong, X.,  
 1270 and Wu, P.: Vertical dependence of horizontal variation of cloud microphysics:  
 1271 observations from the ACE-ENA field campaign and implications for warm-rain simulation  
 1272 in climate models, Atmos. Chem. Phys., 21, 3103-3121, 10.5194/acp-21-3103-2021, 2021.  
 1273 Zheng, Q. and Miller, M. A.: Summertime Marine Boundary Layer Cloud, Thermodynamic,  
 1274 and Drizzle Morphology over the Eastern North Atlantic: A Four-Year Study, Journal of  
 1275 Climate, 35, 4805-4825, <https://doi.org/10.1175/JCLI-D-21-0568.1>, 2022.  
 1276 Zheng, X., Dong, X., Xi, B., Logan, T., and Wang, Y.: Distinctive aerosol-cloud-precipitation  
 1277 interactions in marine boundary layer clouds from the ACE-ENA and SOCRATES aircraft  
 1278 field campaigns, EGUsphere, 2023, 1-45, 10.5194/egusphere-2023-2608, 2023.  
 1279 Zheng, X., Xi, B., Dong, X., Wu, P., Logan, T., and Wang, Y.: Environmental effects on  
 1280 aerosol–cloud interaction in non-precipitating marine boundary layer (MBL) clouds over  
 1281 the eastern North Atlantic, Atmos. Chem. Phys., 22, 335-354, 10.5194/acp-22-335-2022,  
 1282 2022.  
 1283 Zheng, X., Qiu, S., Zhang, D., Adebisi, A. A., Zheng, X., Faruque, O., Tao, C., and Wang, J.:  
 1284 Variability of Eastern North Atlantic Summertime Marine Boundary Layer Clouds and  
 1285 Aerosols Across Different Synoptic Regimes Identified with Multiple Conditions, ESS Open  
 1286 Archive, 10.22541/essoar.172434363.30466798/v1, 2024.

1287 Zheng, Y., Zhu, Y., Rosenfeld, D., and Li, Z.: Climatology of Cloud-Top Radiative Cooling in  
1288 Marine Shallow Clouds, Geophysical Research Letters, 48, e2021GL094676,  
1289 <https://doi.org/10.1029/2021GL094676>, 2021.  
1290 Zhou, X. and Feingold, G.: Impacts of Mesoscale Cloud Organization on Aerosol-Induced  
1291 Cloud Water Adjustment and Cloud Brightness, Geophysical Research Letters, 50,  
1292 e2023GL103417, <https://doi.org/10.1029/2023GL103417>, 2023.

1293

1294

1295

1296

1297  
1298

Table 1. WRF physics scheme configuration

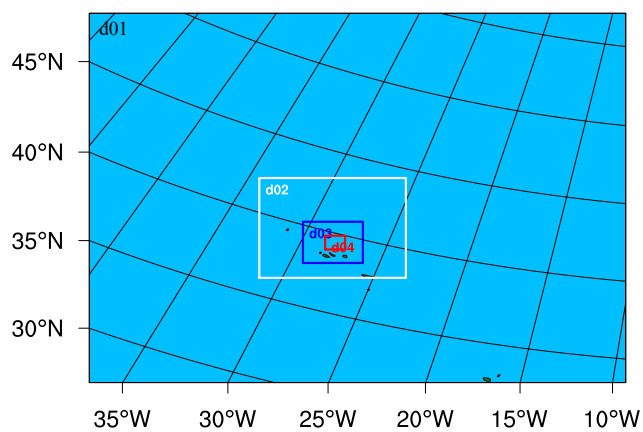
Physics Processes	Scheme	Reference
Microphysics	Morrison (2 moments) scheme	Morrison et al. (2009)
Longwave radiation	RRTMG scheme	Mlawer et al. (1997)
Shortwave radiation	RRTMG scheme	Iacono et al. (2008)
Surface-layer	Monin-Obukhov surface layer	Monin and Obukhov (1954)
Land surface	Unified Noah land-surface model	Chen and Dudhia (2001)
Planetary boundary layer	MYJ (Eta) TKE scheme (d01 and d02 only)	Mellor and Yamada (1982) Janjić (1994)
Shallow cumulus parameterization	GRIMS scheme (d01 and d02 only)	Hong and Jang (2018)

1299  
1300  
1301



Table 2. Ten-minute mean and standard deviation of cloud condensation nuclei (CCN), liquid water path (LWP), cloud droplet number (Nc), cloud radius (Re), and rainfall intensity (RI) over three study cases. Data are averaged over ~25 km of the domain 4 and total 16 averaged grids are in the domain 4. Rain and non-rain are averaged the grids when the RI on the grid is larger than and equal to zero, respectively. Only CCN are averaged within 1000 m height over the domain 4, other variables are averaged within 2000 m height.

Area	Case	CCN (cm <sup>-3</sup> )	LWP (g m <sup>-2</sup> )	Nc (cm <sup>-3</sup> )	Re (μm)	RI (mm hr <sup>-1</sup> )
Domain	Control	73.07 ± 48.77	53.17 ± 32.65	22.68 ± 11.59	9.97 ± 2.31	0.009 ± 0.033
	Perturbed	286.88 ± 183.69 (+293%)	79.25 ± 56.62 (+49%)	59.74 ± 27.29 (+163%)	7.83 ± 2.02 (-21%)	0.008 ± 0.033 (-11%)
Rain	Control	68.15 ± 48.05	58.57 ± 31.69	20.17 ± 9.33	10.47 ± 2.07	0.011 ± 0.035
	Perturbed	250.14 ± 153.23 (+267%)	91.81 ± 55.06 (+57%)	53.01 ± 20.39 (+163%)	8.35 ± 1.83 (-20%)	0.009 ± 0.036 (-18%)
Non-Rain	Control	103.73 ± 41.52	18.91 ± 9.81	38.57 ± 11.93	6.81 ± 0.76	0 ± 0
	Perturbed	444.47 ± 217.08 (+328%)	24.22 ± 15.80 (+28%)	89.24 ± 33.42 (+131%)	5.54 ± 0.90 (-19%)	0 ± 0



1309  
1310  
1311  
1312

Figure 1. Model domains are designed for simulations. The 4 domains ~~denote~~ 4 horizontal ~~resolutions~~ of 5 km (d01), 1.67 km (d02), 0.56 km (d03), and 0.19 km (d04), respectively.

Deleted: with  
Deleted: resolution

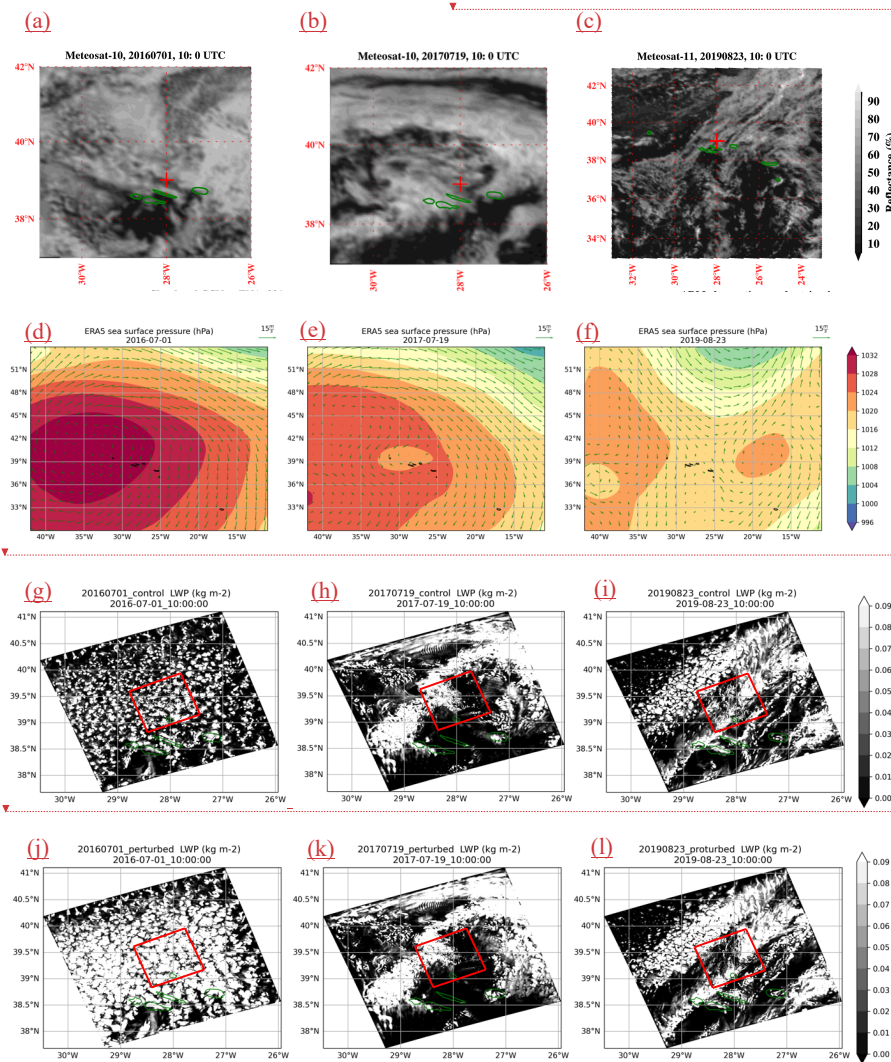
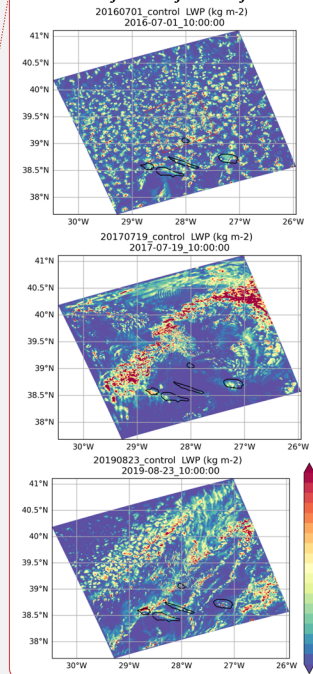


Figure 2. Spinning Enhanced Visible Infra-Red Imager (SEVIRI) images from the Meteosat satellite at 10:00 UTC on (a) 1 July 2016, (b) 19 July 2017, and (c) 23 August 2019 over the ENA. (d), (e), and (f) are on the same day of (a), (b), and (c), respectively, but from the ERA5 mean sea surface pressure (contour; units: hPa) and 10-meter surface wind (arrow; units:  $\text{m s}^{-1}$ ).

Deleted: <object><object>  
<object>

Deleted: <object><object><object><object><object>  
<object>

Deleted: <object><object><object>



Deleted: they are

1333 (g), (h), and (i) are on the same day of (a), (b), and (c), respectively, but ~~from the~~ WRF-Chem  
1334 simulated liquid water path (LWP; units: kg m<sup>-2</sup>) in the control runs, ~~while (j), (k), and (l) are in~~  
1335 ~~the perturbed runs~~. The red boxes in the figures indicate the result from domain 4.

Deleted: they are

Deleted: .

Deleted: the

1336

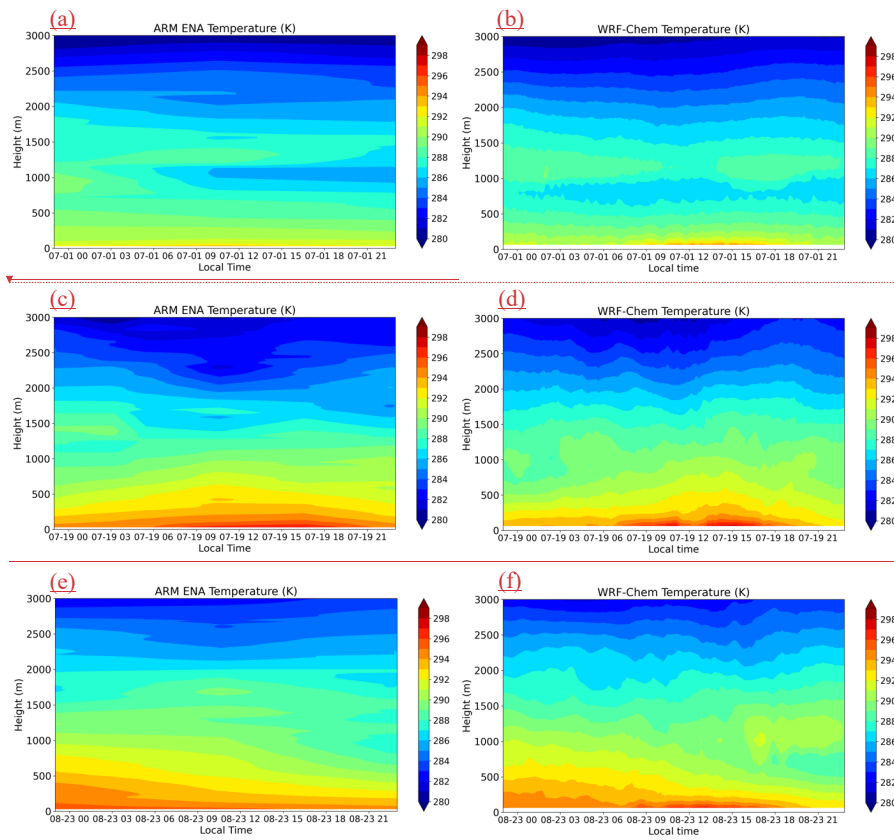
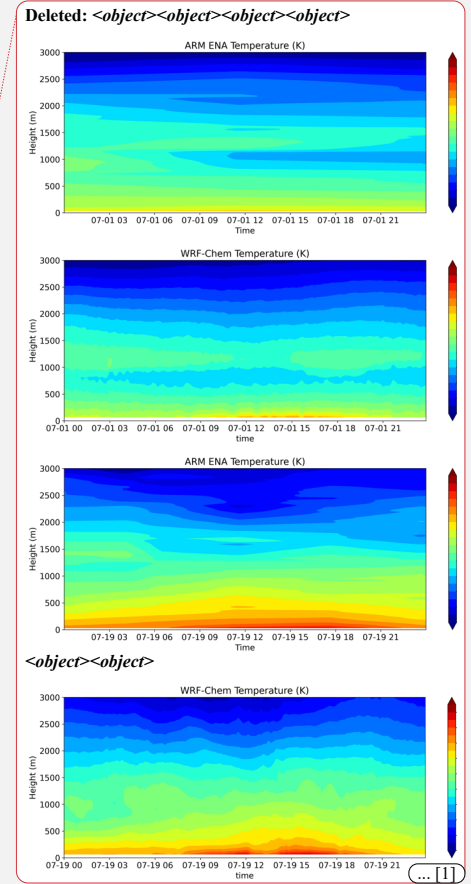


Figure 3. The time series (local time; UTC -1 hour) of temperature profiles (units: K) from ARM interpolated soundings at the Azores (39.09°N, -28.02°W) on (a) 1 July 2016, (c) 19 July 2017, and (e) 23 August 2019. Panels (b), (d), and (f) depict the same dates as (a), (c), and (e), respectively, but show the average temperature from WRF-Chem simulated results over  $20 \times 20$  grids centered on the Azores (approximately 4 km resolution).



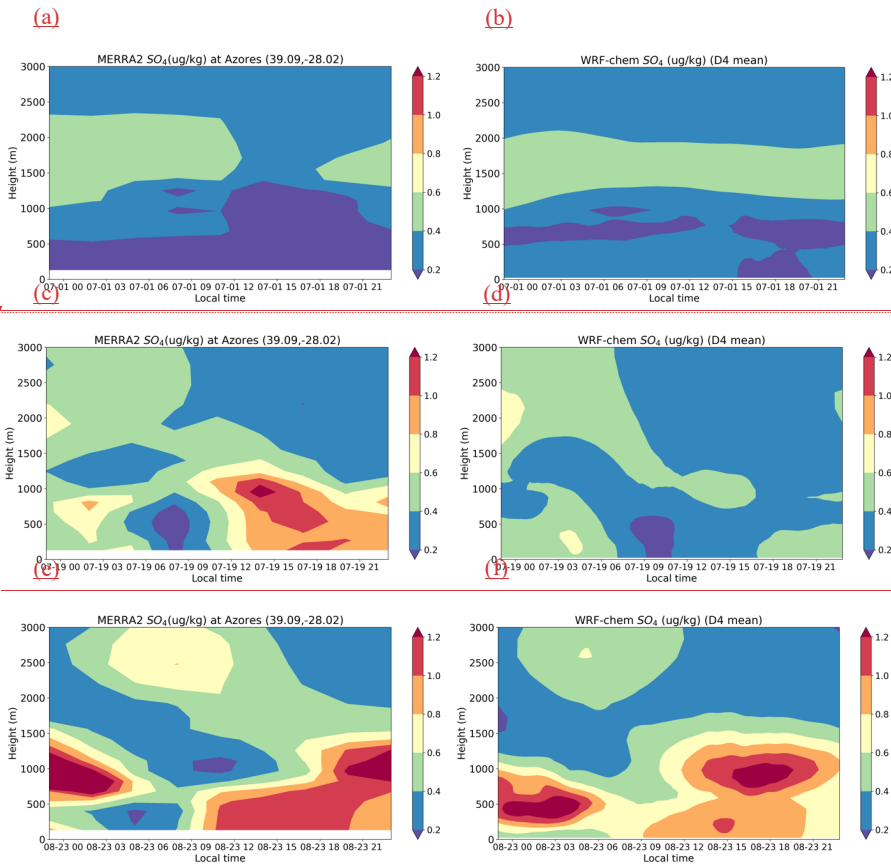
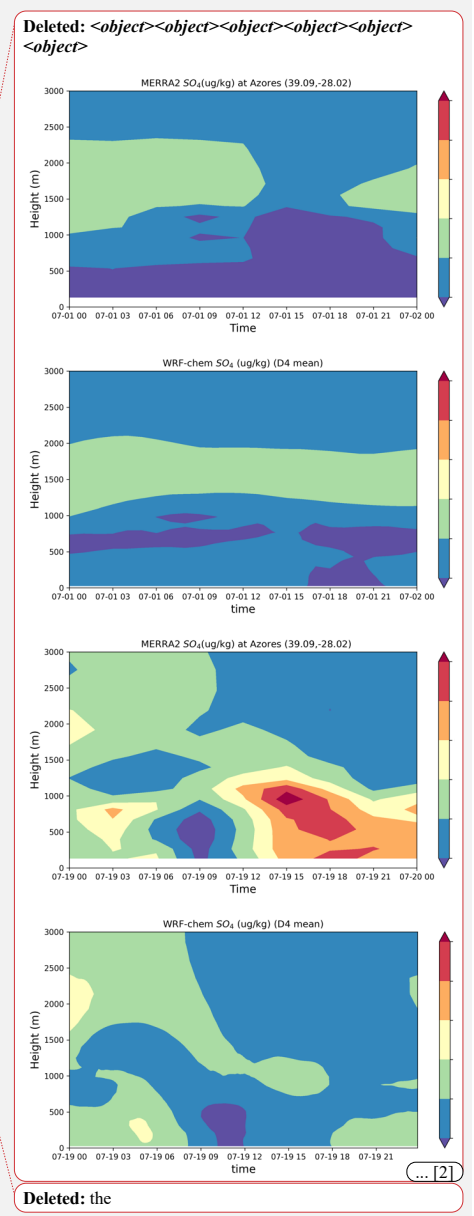
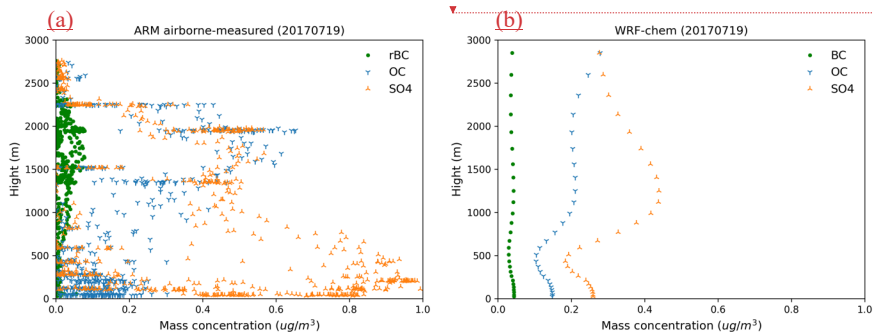


Figure 4. The time series (local time; UTC – 1 hour) of  $\text{SO}_4$  profiles (units:  $\mu\text{g kg}^{-1}$ ) from MERRA-2 at the Azores (39.09°N, -28.02°W) on (a) 1 July 2016, (c) 19 July 2017, and (e) 23 August 2019. Panels (b), (d), and (f) depict the same dates as (a), (c), and (e), respectively, but show the average aerosol concentration from WRF-Chem simulated data over domain 4.



1379



1380  
1381  
1382  
1383  
1384  
1385  
1386  
1387  
1388  
1389

Figure 5. (a) ARM airborne-measured vertical profiles of SO<sub>4</sub>, OC and refractory BC (rBC) mass concentration (units:  $\mu\text{g cm}^{-3}$ ) averaged over multiple flights on 19 July 2017. **Note** that the highly uncertain and noisy aerosol observations between 600 – 1000 m height due to cloud contamination. (b) WRF-Chem simulated vertical profile of SO<sub>4</sub>, OC, and BC mass concentration (units:  $\mu\text{g cm}^{-3}$ ) averaged over domain 4 during the flight time from 8:40 to 11:50 UTC.

Deleted: <object><object>

Deleted: Noted

Deleted: the

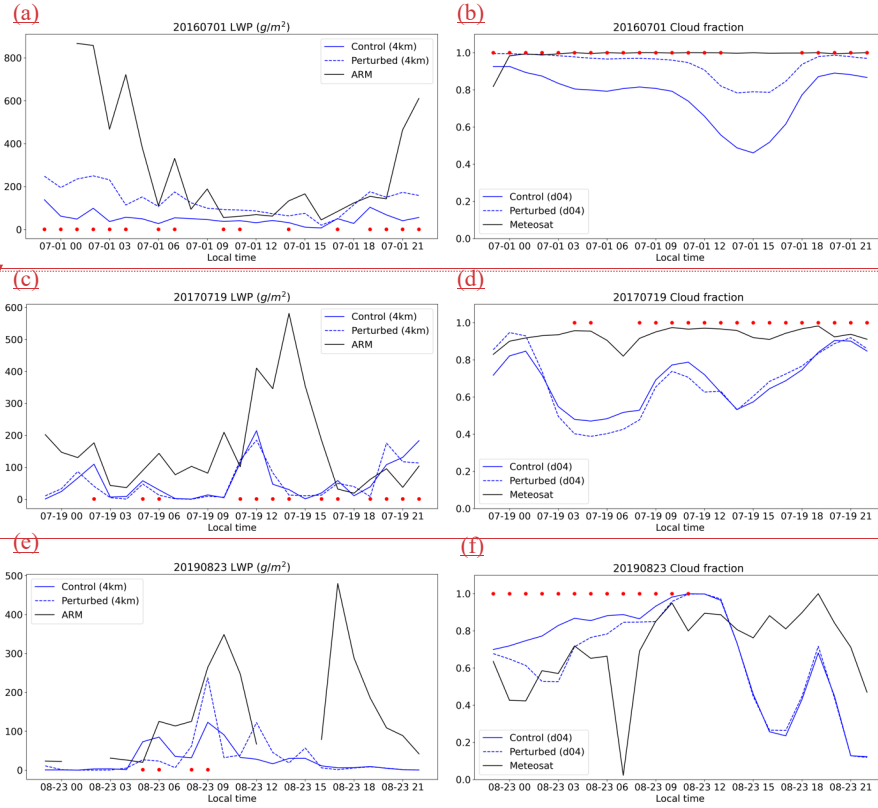
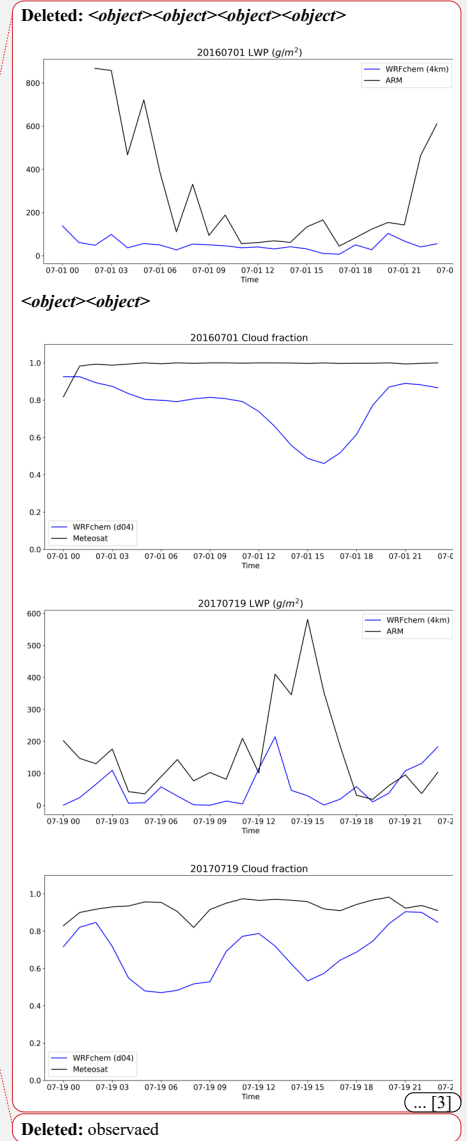


Figure 6. (a), (c), and (e) are the hourly time series (local time; UTC - 1 hour) of 4 km-averaged (4km) liquid water path (units:  $\text{g m}^{-2}$ ) simulated from WRF-Chem (blue solid line) and observed from ARM (black solid line) on 1 July 2016, 19 July 2017, and 23 August 2019, respectively. (b), (d), and (f) are the hourly time series of domain-averaged (d04) cloud fraction simulated from WRF-Chem (blue solid line) and observed from Meteosat (black solid line) on 1 July 2016, 19 July 2017, and 23 August 2019, respectively. The 4 km-averaged data are averaged from the model simulated results over  $20 \times 20$  grids centered on the Azores (approximately 4 km resolution). The red dots indicate when rainfall intensity is higher than  $0.001$  ( $0.01$ )  $\text{mm hr}^{-1}$  in 4-km averaged area (domain 4).





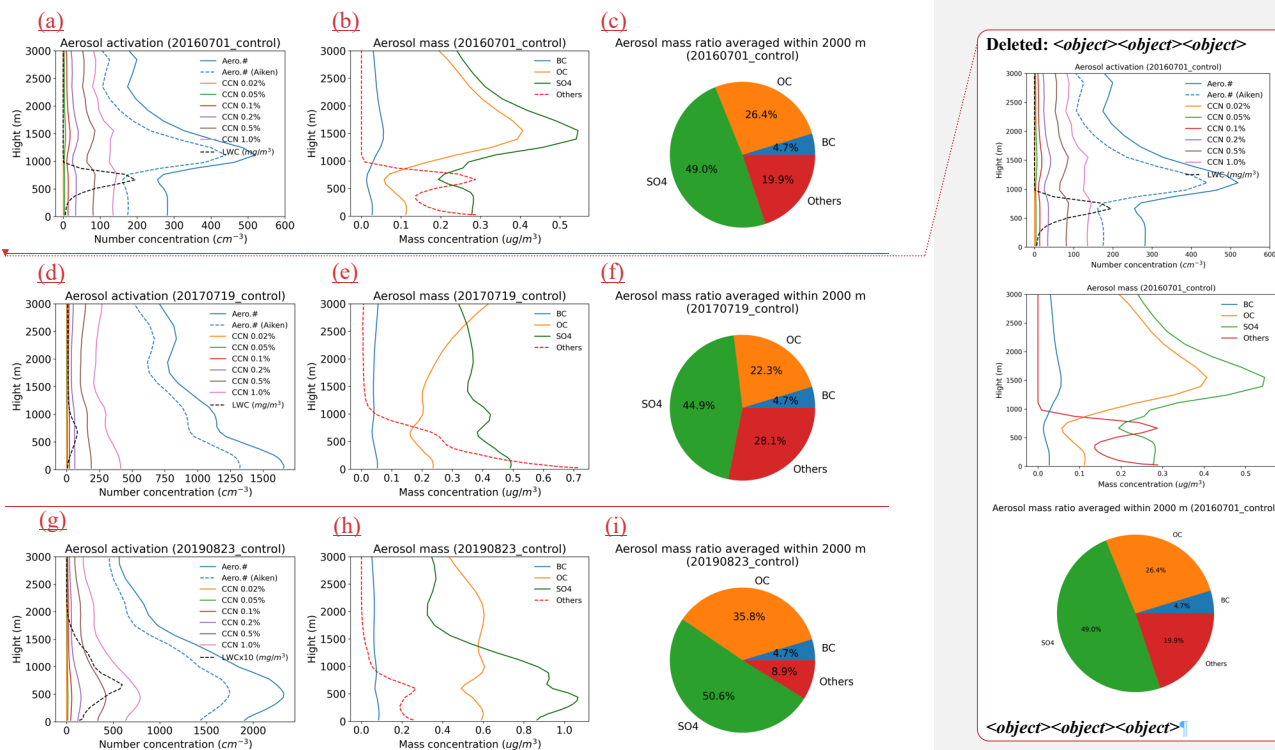


Figure 7. (a), (d), and (g) WRF-Chem vertical profiles of aerosol number concentration (Aiken mode and accumulation mode; units:  $\text{cm}^{-3}$ ), aerosol number concentration (Aiken mode only; units:  $\text{cm}^{-3}$ ), CCN number concentration below different supersaturations (units:  $\text{cm}^{-3}$ ), and liquid water content (cloud and rain; units:  $\text{mg m}^{-3}$ ) averaged over the domain 4 on 1 July 2016, 19 July 2017, and 23 August 2019, respectively, in the control runs. (b), (e), and (h) WRF-Chem vertical profiles of BC, OC, SO<sub>4</sub>, and other species (like sea salt) (units:  $\mu\text{g cm}^{-3}$ ) averaged over the domain 4 on 1 July 2016, 19 July 2017, and 23 August 2019, respectively, in the control runs. (c), (f), and (i) Pie chart of aerosol mass of different species averaged within 2000 m height on 1 July 2016, 19 July 2017, and 23 August 2019, respectively, in the control runs. Note that LWC is adjusted to fit the scale of x-axis for each case.

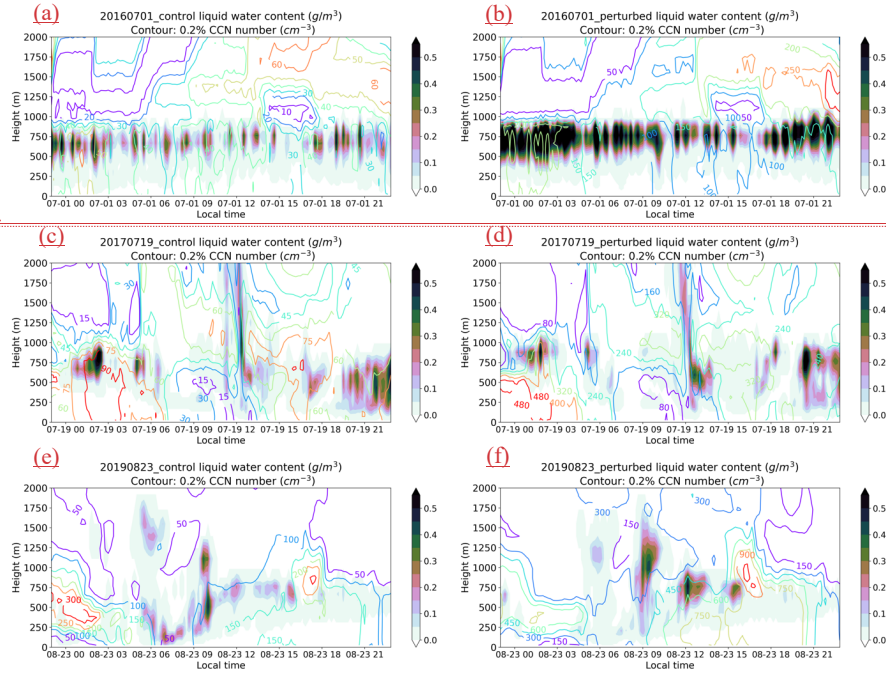
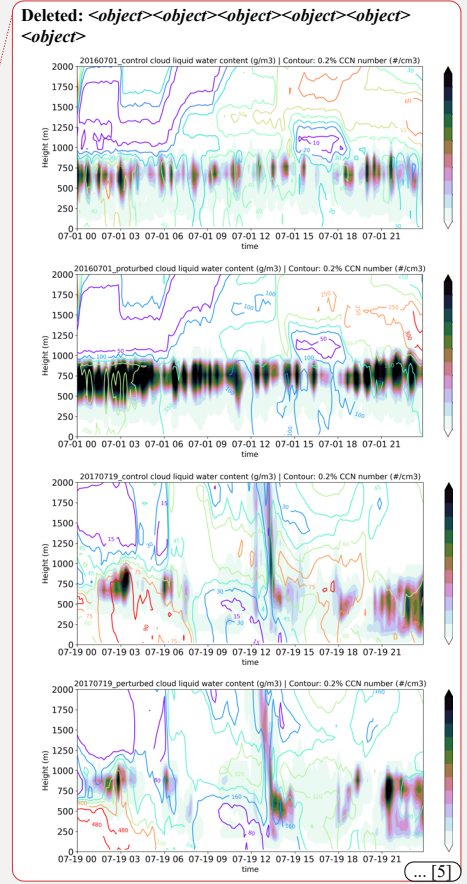


Figure 8. (a), (c), and (e) are the time series (local time: UTC – 1 hour) of 4 km-averaged cloud liquid water content profile (shade; units:  $\text{g cm}^{-3}$ ) and CCN (0.2% supersaturation) number concentration profile (contour; units:  $\# \text{ cm}^{-3}$ ) on 1 July 2016, 19 July 2017, and 23 August 2019, respectively, in the control runs. (b), (d), and (f) are the same as (a), (c), and (e), respectively, but in the perturbed runs. The data are averaged from the model simulated results over  $20 \times 20$  grids centered on the Azores (approximately 4 km resolution).



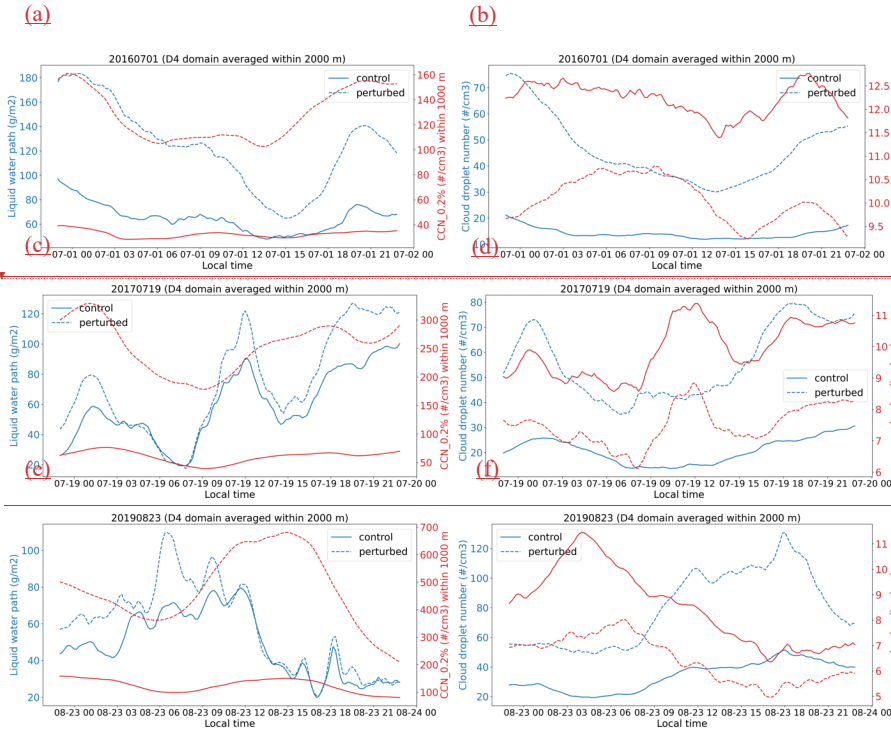
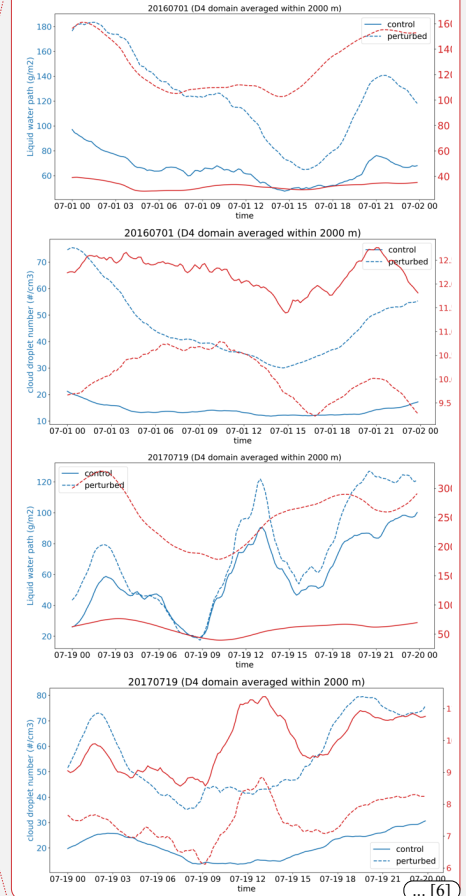


Figure 9. (a), (c), and (e) are the time series of domain-averaged liquid water path (blue lines; units:  $\text{g m}^{-2}$ ) and CCN number concentration below 0.2% supersaturation (red lines; units:  $\# \text{ cm}^{-3}$ ) for the control case (solid lines) and the perturbed case (dashed lines) on 1 July 2016, 19 July 2017, and 23 August 2019, respectively. (b), (d), and (f) are the time series of domain-averaged cloud droplet number (blue lines; units:  $\# \text{ cm}^{-3}$ ) and cloud radius (red lines; units:  $\mu\text{m}$ ) for the control (solid lines) and perturbed (dashed lines) on 1 July 2016, 19 July 2017, and 23 August 2019, respectively. Only CCN data are averaged within 1000 m height over domain 4, other variables are averaged within 2000 m height.

Deleted: <object><object><object><object><object>  
<object>



Deleted: under

Deleted: the

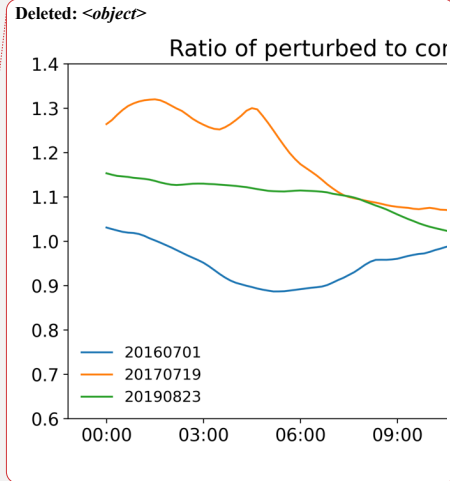
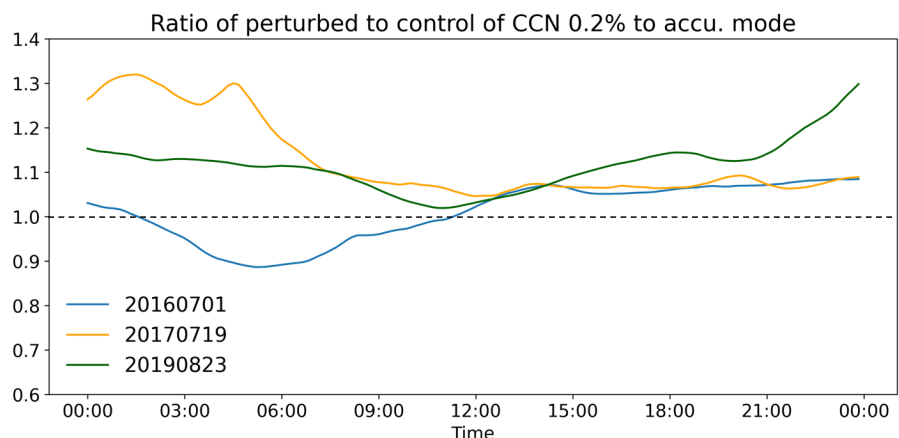
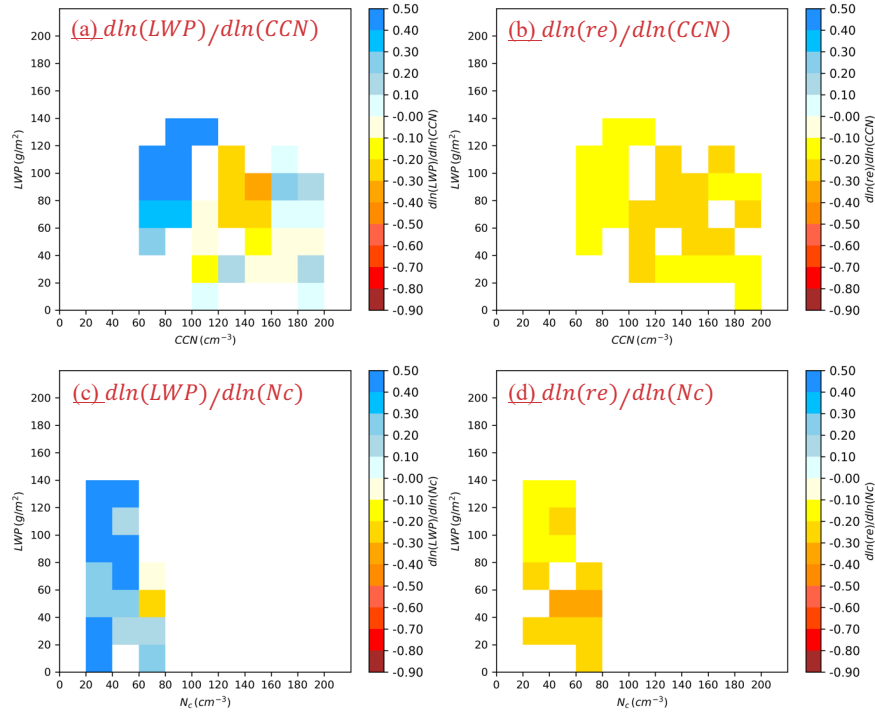


Figure 10. The time series of the ratio of the number concentration of CCN at a supersaturation of 0.2% in the perturbed runs to that in the control runs, normalized by the corresponding accumulation mode aerosol concentration, defined as  $(CCN_{0.2\%}/Accu.aerosols)_{perturbed} / (CCN_{0.2\%}/Accu.aerosols)_{control}$ . The black dashed line indicates the value of unity.

- Deleted: percentage
- Deleted: activated
- Deleted: 0.2%
- Deleted: to
- Deleted: to the
- Deleted: aerosols between perturbed and control runs.
- Deleted: back
- Deleted: 1.0



Deleted: <object><object><object><object>

1525

1526 Figure 11. (a) and (b) are the mean liquid water path (LWP) and cloud radius (Re)  
 1527 susceptibilities for different cloud condensation nuclei (CCN) and LWP bins for three study  
 1528 cases, respectively. (c) and (d) are the same as (a) and (b), respectively, but for different cloud  
 1529 droplet number (Nc) and LWP bins. The logarithmic slope between LWP and CCN, denoted as  
 1530 ( $d\ln(LWP)/d\ln(CCN)$ ), is calculated at each output time (every 10 minutes) using data from 16  
 1531 aggregate grid points ( $\sim 25$  km for each grid point) from the control run and 16 aggregated grid  
 1532 points from the perturbed run.

1533

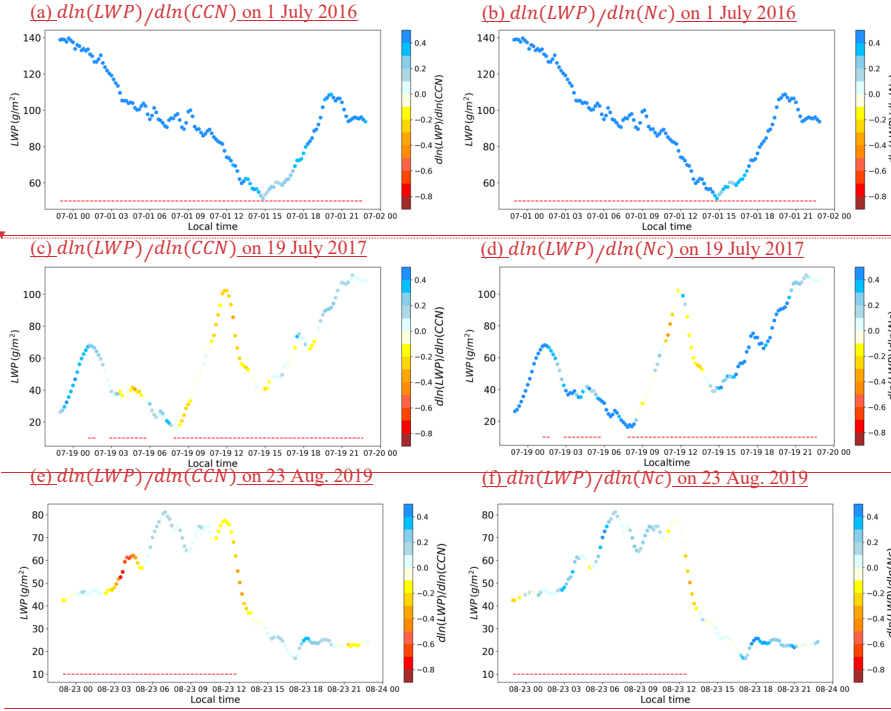
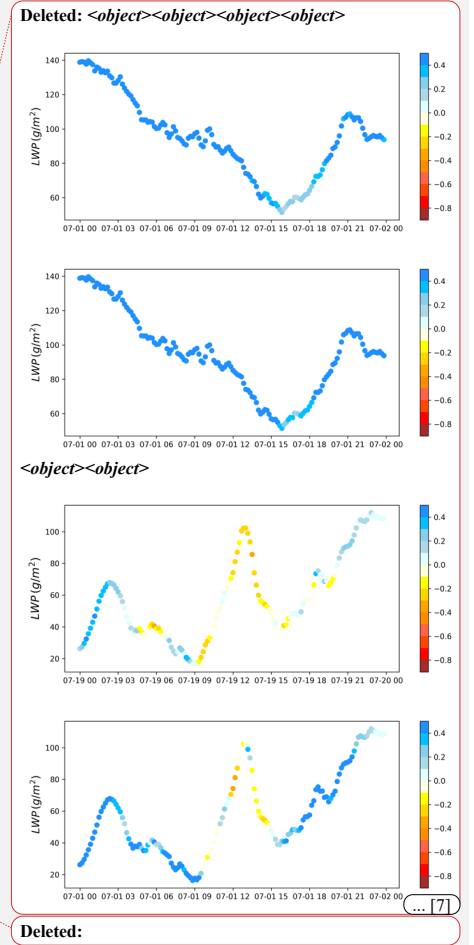
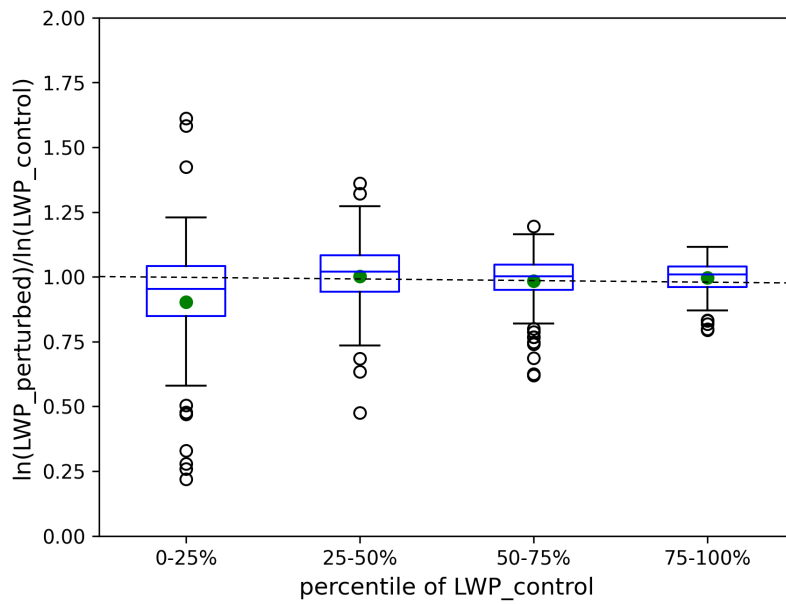


Figure 12. (a), (c) and (e) are the time variable of LWP susceptibility for different CCN concentration, denoted as  $(d\ln(LWP)/d\ln(CCN))$ , on 1 July 2016, 19 July 2017, and 23 August 2019, respectively. (b), (d) and (f) are the time variable of LWP susceptibility for different Nc concentration, denoted as  $(d\ln(LWP)/d\ln(Nc))$ , on 1 July 2016, 19 July 2017, and 23 August 2019, respectively. The logarithmic slope between LWP and CCN is calculated at each output time (every 10 minutes) using data from 16 aggregate grid points (~25 km for each grid point) from the control run and 16 aggregated grid points from the perturbed run. The red dashed lines indicate when rainfall intensity is higher than  $0.001 \text{ mm } 10\text{-min}^{-1}$  in domain 4.





1563

1564 Figure 13. **Boxplot** of the relative change in  $\ln(LWP)$  between the perturbed and control cases  
 1565 across different LWP **Percentile** ranges in the control case during the negative susceptibility for  
 1566 LWP shown in Fig. 12. The box extends from the first quartile to the third quartile of the data,  
 1567 with a line at the median. The whiskers extend from the box to the farthest data point lying  
 1568 within 1.5x the inter-quartile range from the box. **Outlier values** are those past the end of the  
 1569 whiskers. Green dots are the mean value, and the back dashed line indicates the value of 1.0.

1570

Deleted: The boxplot

Deleted: percentile

Deleted: Flier points

▼	Page 49: [1] Deleted	Lee, Hsiang-He	2/3/25 8:31:00 PM
▼	Page 50: [2] Deleted	Lee, Hsiang-He	2/3/25 8:31:00 PM
▼	Page 52: [3] Deleted	Lee, Hsiang-He	2/3/25 8:31:00 PM
▼	Page 53: [4] Deleted	Lee, Hsiang-He	2/3/25 8:31:00 PM
▼	Page 54: [5] Deleted	Lee, Hsiang-He	2/3/25 8:31:00 PM
▼	Page 55: [6] Deleted	Lee, Hsiang-He	2/3/25 8:31:00 PM
▼	Page 58: [7] Deleted	Lee, Hsiang-He	2/3/25 8:31:00 PM
▼			